Renewable and Sustainable Energy Reviews 194 (2024) 114304

Contents lists available at ScienceDirect

Renewable and Sustainable Energy Reviews

journal homepage: www.elsevier.com/locate/rser

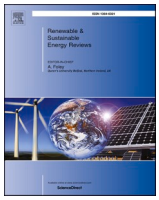

Pristine and engineered biochar as Na-ion batteries anode material: A comprehensive overview

Mattia Bartoli [a,b,i], Alessandro Piovano [a,i,*], Giuseppe Antonio Elia [a,i], Giuseppina Meligrana [a,i], Riccardo Pedraza [a,h,i], Nicolò Pianta [c,i], Cristina Tealdi [d,i], Gioele Pagot [e,i], Enrico Negro [e,i], Claudia Triolo [f,i], Lourdes Vazquez Gomez [g,i], Nicola Comisso [g,i], Alberto Tagliaferro [a,i], Saveria Santangelo [f,i], Eliana Quartarone [d,i], Vito Di Noto [e,i], Piercarlo Mustarelli [c,i], Riccardo Ruffo [c,i], Claudio Gerbaldi [a,i,**]

[a] Department of Applied Science and Technology (DISAT), Politecnico di Torino, Corso Duca degli Abruzzi 24, 10129, Torino, Italy
[b] Center for Sustainable Future Technologies (CSFT), Istituto Italiano di Tecnologia (IIT), Via Livorno 60, 10144, Torino, Italy
[c] Department of Materials Science, University of Milano-Bicocca, Via Cozzi 55, 20125, Milano, Italy
[d] Department of Chemistry, University of Pavia, Viale Taramelli 16, 27100, Pavia, Italy
[e] Section of Chemistry for the Technology (ChemTech) and INSTM, Dept. of Industrial Engineering, University of Padova, Via Marzolo 9, I-35131, Padova (PD), Italy
[f] Dipartimento di Ingegneria Civile, dell'Energia, dell'Ambiente e dei Materiali (DICEAM), Università "Mediterranea", Via Zehender, Loc. Feo di Vito, 89122, Reggio Calabria, Italy
[g] Istituto di Chimica della Materia Condensata e di Tecnologie per l'Energia (ICMATE), Consiglio Nazionale delle Ricerche (CNR), C.so Stati Uniti 4, 35127, Padova, Italy
[h] Department of Mechanical and Aerospace Engineering (DIMEAS), Politecnico di Torino, Corso Duca degli Abruzzi 24, 10129 Turin, Italy
[i] National Reference Center for Electrochemical Energy Storage (GISEL) - INSTM, Via G. Giusti 9, 50121, Firenze, Italy

ARTICLE INFO

Keywords:
Biochar
Hard carbon
Anode
Sodium ion battery
Sustainable energy

ABSTRACT

The sodium-ion battery (Na-ion battery, NIB) is considered the most promising post-lithium energy storage technology, taking advantage of using the same manufacturing technology as Li-ion batteries (LIBs), while enabling the use of more abundant and economic, thus more sustainable, raw materials. Due to the inability of Na^+ ions to be intercalated within the graphene-layered structure of graphite-based electrodes (the state of art anode material in LIBs), highly disordered and microporous carbons, known as hard carbons, are considered the anode material of choice for NIB technology. Biomass-derived biochar (BC) is one of the most relevant classes of hard carbons, exhibiting a good combination of sustainable fabrication, structural-morphological features and electrochemical performances. In this review, the main achievements on BC are rigorously reported from the production to the application into NIBs, with particular emphasis on the strategies to improve the electrochemical behaviour of BC by activating it and tailoring its chemical and structural properties. These strategies include selecting specific feedstocks, modulation of the pyrolysis temperature, pre- and post-production treatments, and materials engineering. The possible role of BC in sustainable NIBs development is also briefly discussed, together with some insights of its use in other post-Li energy storage systems and some concluding remarks and future direction of the research.

1. Introduction

One of the bold and transformative steps being urgently needed by our modern society to face the dramatic worldwide consequences of climate changes, thus shifting the world onto a sustainable place, is the transition from mobility based on fossil fuels to electric vehicles (see the UN 2030 Agenda for Sustainable Development or the European Green Deal) [1]. Accordingly, the development of new generation electrochemical storage systems has become a crucial task to be accomplished in the near future. During the last decades, lithium-ion batteries (LIBs) have gained the attention of both academia and industry, spreading

* Corresponding author. Department of Applied Science and Technology (DISAT), Politecnico di Torino, Corso Duca degli Abruzzi 24, 10129, Torino, Italy.
** Corresponding author. Department of Applied Science and Technology (DISAT), Politecnico di Torino, Corso Duca degli Abruzzi 24, 10129, Torino, Italy
E-mail addresses: alessandro_piovano@polito.it (A. Piovano), claudio.gerbaldi@polito.it (C. Gerbaldi).

https://doi.org/10.1016/j.rser.2024.114304
Received 28 June 2023; Received in revised form 25 January 2024; Accepted 28 January 2024
Available online 12 February 2024

Acronyms and abbreviations

ATR	Attenuated total reflectance
BC	Biochar or biomass-derived carbon
BES	Broadband electrical spectroscopy
BET	Brunauer-Emmett-Teller
BJH	Barrett-Joyner-Halenda
CE	Coulombic efficiency
CNT	Carbon nanotube
COP26	2021 United Nations climate change conference
CRM	Critical raw material
CV	Cyclic voltammetry
CVD	Chemical vapour deposition
CVF	Crystalline volume fraction
DFT	Density functional theory
DMA	Dynamic mechanical analysis
DRIFTS	Diffuse reflectance infrared Fourier transformed spectroscopy
EIS	Electrochemical impedance spectroscopy
ESR	Electron spin resonance
EPR	Electron paramagnetic resonance
EV	Electric vehicle
FT-IR	Fourier transformed infrared spectroscopy
GCMC	Grand canonical Monte Carlo
GHG	Greenhouse gas
H/C	Hydrogen/Carbon
HC	Hard carbon
IPCC	Intergovernmental panel on climate change
KIB	K-ion battery, potassium-ion battery
LIB	Li-ion battery, lithium-ion battery
Li–O_2	Lithium–Oxygen or Lithium-air battery
Li–S	Lithium-Sulphur battery
MD	Molecular dynamics
MDSC	Modulated differential scanning calorimetry
MOF	Metal organic framework
NIB	Na-ion battery, sodium-ion battery
NOP-BC	Nitrogen, oxygen and phosphorus co-doped biochar
O/C	Oxygen/Carbon
PDFs	Pair distribution functions
RS	Reflectance spectroscopy
SEI	Solid electrolyte interphase
ReaxFF	Reactive force field
SHE	Standard hydrogen electrode
UV	Ultraviolet
XAS	X-ray absorption spectroscopy
XPS	X-ray photoelectron spectroscopy
XRD	X-ray diffraction

from laboratory to almost every high-tech device [2,3]. As a direct consequence, lithium reserves are becoming shorter year by year, and their price is rising at the same time [4]. Therefore, the need for post-LIBs technologies is increasingly more compelling, and sodium-ion batteries (NIBs) are among the most promising systems, considering that Na is widely abundant, equally distributed on Earth, and exhibits similar chemistry to that of Li; some limitations to NIBs development are constituted by the need of new specific materials for the electrodes, the energetically less favourable intercalation of Na^+ into a fixed positive electrode with respect to Li^+ (limiting the overall cell voltage and, hence, the energy density), slower kinetics, possible side reactions with the electrolyte (limiting the cycle stability), generally lower initial coulombic efficiency and higher cell volume expansion [5–8]. In recent years, the technological gap between LIBs and NIBs has been narrowing, with many companies (Novasis Energies, Faradion, Natron Energy, Rechargion Energy, HiNa, Altris, TIAMAT, AGM, Contemporary Amperex Technology Co., Ltd. - CATL) declaring to be close to commercialization of NIBs [9–11], as summarized in Table 1 [12]. Most notably, Northvolt (Sweden) announced at the end of 2023 of having officially inserted into its cell portfolio a NIB based on Altris AB technology, enabling the worldwide expansion of cost-efficient and sustainable energy storage systems to afford the expected global electrification based on renewable power sources [13].

On the positive electrode side, many different chemistries are considered, including layered transition metal oxides, Prussian white, or vanadium phosphates; whereas on the negative electrode side, hard carbons have shown the best combination of performances and workability [14–17]. In particular, the carbon produced by biomass pyrolysis, known as biochar (BC), represents a solution that combines a sustainable productive methodology and good electrochemical behaviour [18–20]. BC properties must be finely tuned to match the requirements of marketable energy storage devices. Due to the great variety of BC production and tailoring approaches, the need of a comprehensive overview on the use of BC as anode material for NIBs is crucial, aiming at considering all the possible strategies proposed in literature.

As reported in Fig. 1S, the interest of the scientific community on BC applied to energy storage is exponentially growing from about 2015, mostly related to the development of NIBs, but in part also to the development of other post-Li technologies.

Despite some reviews have already pointed out the beneficial role of biochar in energy storage devices [18,19], the scientific literature on this topic still suffers the lack of uniformity among the reported studies in terms of prepared materials, post-synthesis treatments, and conditions of electrochemical testing, thus constituting an obstacle for all the researchers who are going to approach it for the first time. Therefore, this review article aims at systematically discussing the application of biochar into NIBs and other post-Li technologies, comparing as much as possible the results obtained by different research groups and

Table 1
List of the companies working on the commercialization of NIBs, adapted and reproduced from Hasa et al. [12].

Company	NIB Cell Positive//Negative	Current Wh/kg	Available Formats	Expected Markets
Faradion (UK), AMTE (UK), INDI-Energy (India), Natrium Energy (China)	Na Layered Oxide//HC	120–160 135–140 120–150 130–160	Pouch, Prismatic	Energy – including Telecoms, mobility, back-up, UPS, ESS, Renewables
HiNa Battery (China)	Na Layered Oxide//Soft Carbon	120–145	Pouch	Energy - mobility, back-up, UPS, ESS, Renewables
CATL (China)	Prussian-White Analogue//HC	160	Pouch	Grid, stationary, UPS
Tiamat Energy (France)	$Na_3V_2(PO_4)_2F_3$//HC	80–100	Cylindrical	Power markets, hybrid buses, Power tools
Altris AB (Sweden)	Prussian-Blue Analogue//HC	100–120	Pouch	Energy markets
Natron Energy (USA)	Prussian-Blue Analogue: Fe//Mn	25-40 (50 Wh/l)	Pouch	Data centers, back-up

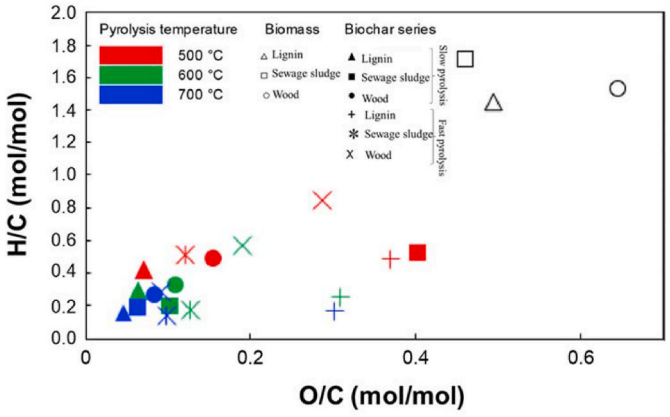

Fig. 1. Van Krevelen diagram showing the effect of processing temperature on BC. Picture readapted and reprinted with permission (CC BY-NC-ND 4.0) from Bartoli et al. [21].

extrapolating the correlation between the chemical and structural properties of the materials and their electrochemical performances, so that it could serve as a guideline for further discoveries and developments.

2. BC production and engineering

2.1. BC production

BC is produced through thermochemical cracking of biomasses under different conditions. The main routes for BC production are torrefaction, pyrolysis and gasification. The main and more relevant difference between these above-mentioned routes is represented by the different temperatures reached during the process.

During torrefaction, the temperature rises to 200–350 °C achieving only partial carbonisation of biomass [22]. Solid recovered from biomass torrefaction generally presents a C content of up to ≈50 wt% with a yield of up to 70 % [23]. An improvement in the C content up to 80 wt% can be reached by using microwave heating and additives [24–26]. The technology hardly met the requirement to produce effective anodic materials due to the lack of conductivity.

Increasing the processing temperature above 400 °C, proper pyrolytic processes occur in an oxygen-free atmosphere. While torrefaction promotes a slight degradation of biomass macromolecules, pyrolytic conversion leads to an advance cracking process of lignin, cellulose and hemicellulose with the formation of BC and complex liquid mixtures named bio-oils [27]. Pyrolysis could be run by using different heating technologies [28–30], and apparatus designs [31] with wide variations in product fraction yields quality [32].

Contrary to pyrolysis, gasification occurs in an oxidant atmosphere such as air [33], oxygen or steam [34], generally at temperatures higher than 800 °C with or without the addition of a catalyst [35]. The main gasification output is represented by gas composed of a mixture of carbon monoxide, carbon dioxide, methane, hydrogen and water vapour. Contrary to BC produced from pyrolytic conversions, carbon recovered from stoichiometric gasification is generally very rich in ash and poor in carbon content, discouraging its use for battery applications.

The choice of BC productive way is strictly related to the final use that could require a greater or lower presence of oxygen and hydrogen content, accordingly to Van Krevelen graph as shown in Fig. 1. The structure of BC produced using lignin, sewage sludge, and wood is closely related to both temperature and heating rate. A productive temperature of only 500 °C leads to high H/C and O/C ratios, avoiding using these chars for possible development of anode materials. The carbon content is not the only BC feature relevant to electrochemical applications. Another key parameter is represented by the defective degree of the carbon matrix.

Carbon defectiveness could be quantified by comparing a carbon sample to a perfect graphite and estimating the different arrangements of graphitic domains through several techniques, such as Raman spectroscopy [36], transmission electron microscopy [37] and X-ray powder diffraction [38].

Considering BC thermal evolution, three main stages could be identified and correlated with processing temperature, as sketched in Fig. 2.

First, biomass undergoes proper carbonisation at a temperature ranging from 300 to 400 °C with cracking of its components through complex reaction routes and forming the first aromatic units and releasing small gaseous molecules as H_2O, CO_2 and N_2. In this stage, BC is massively tailored with oxygen-based functionalities (*i.e.*, hydroxyl, carbonyl and carboxylic residues) and displays a highly defective carbon structure. By increasing temperature between 600 and 800 °C, aromatic structures further condense forming proper graphite-like domains still highly disordered but with lesser residual groups. These materials are commonly classified as hard carbon due to their high mechanical hardness [40].

Further temperature increments lead to a progressive enlargement and ordering process of graphitic domains through turbostratic rearrangement [41] that end at a temperature close to 3000 °C when the maximum graphitization degree is reached [42].

The thermal evolution of BC could be easily evaluated by using Raman spectroscopy. Raman spectroscopy is widely utilised to quickly and non-destructively characterise all carbons as they are featured by peculiar and distinct spectral fingerprints [43–45]. Usually, their structural and bonding properties are investigated by studying the scattering excited by a given laser wavelength, whereas complementary information on some specific aspects is inferred by multi-wavelength [46–48].

Visible light (with a wavelength of 532 or 633 nm) is commonly used to carry out single-wavelength Raman analysis [40]. Since the cross-section for sp^3 C–C vibrations is negligible for visible excitation, the visible Raman spectra of carbon materials with mixed sp^3/sp^2 bonding nature are dominated by sp^2 contributions [49]. This is the reason why the nanocrystalline, disordered/amorphous and hard carbons, all containing graphitically ordered nanodomains, exhibit similar visible Raman spectra, consisting of two broad features, the well-known D- and G-bands [50–54] centered at around 1340 and 1580 cm^{-1}, respectively [49,55].

Since the frequency, width and relative intensity of the two bands are sensitive to bonding strength, distribution of bonding lengths and angles, nature and density of defects, Raman spectroscopy is often used, together with complementary characterization techniques, such as transmission electron microscopy [56], to monitor the changes in the microstructure of the graphite-like carbons produced by the variation of their preparation conditions. In order to qualify the nature and quantify the density of defects, the D/G intensity ratio (I_D/I_G), calculated by spectra fitting [36,57,58], is used to estimate the average size of graphitically ordered domains (L_C), *i.e.*, the coherence length [55] that gives a measure of the inter-defect in-plane distance [59].

For hard carbons, the carbonisation temperature (up to 1500 °C) causes the width of the D- and G-bands to decrease and I_D/I_G to increase [51,54,60,61]. As they contain randomly-stacked highly-disordered turbostratic graphitic nanodomain regions cross-linked by amorphous regions with sp^3 bound sites [62,63], these spectral changes are indicative of the narrowing of the distribution of bonding lengths and angles and of the conversion of non-sp^2 to sp^2 defects [47,64], which only contribute to the D-band intensity, *i.e.*, of the evolution towards a less disordered structure, with increased probability of finding sixfold rings in the C clusters [49]. At high carbonisation temperatures, increasing carbonisation time causes only I_D/I_G to decrease [54]. This signals the increase of L_C, *i.e.*, the reduction of the density of sp^2 defects in the basal planes, resulting in higher graphitization degree/development of the

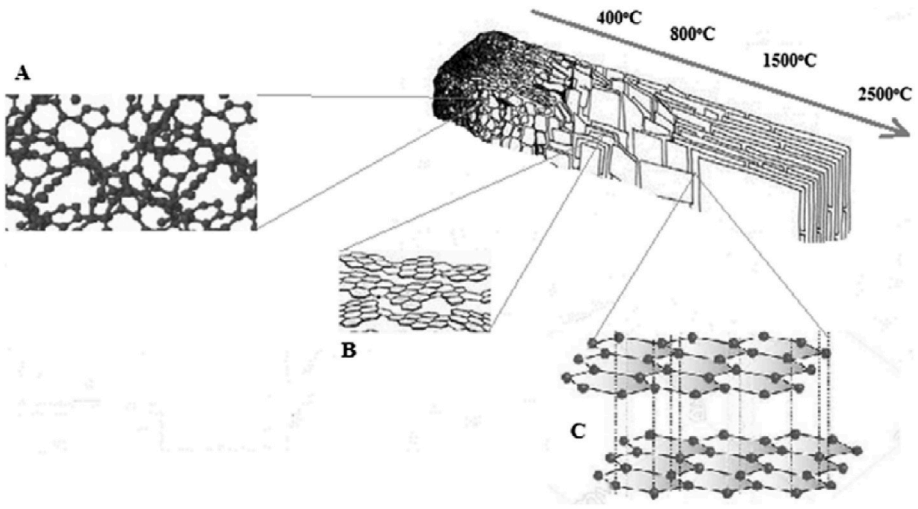

Fig. 2. Thermal evolution of BC structure considering (A) totally amorphous materials produced at low temperature, (B) hard carbon produced from 800 °C and (C) soft carbon produced by using high annealing temperature. Picture was reprinted under CC BY 4.0 license from Tomczyk et al. [39].

turbostratic graphitic nanodomains [65].

The details of the short-range crystal structure of the BCs are extremely important to prompt a facile and reversible uptake of Na^+ species in the anode of a NIB. The distance between the graphitic layers of a BC is larger than that of conventional graphite allowing the reversible intercalation/de-intercalation of bulky Na^+ species. Such *"larger"* distance can be established by a variety of approaches, including: (i) pre-oxidation of the BC [66]; or (ii) introduction of bulky heteroatoms (*e.g.*, P) in each graphitic layer [67] or of nanometric templates (*e.g.*, MgO) between the graphitic layers [68]. X-ray diffraction is a very suitable technique to gauge the distance between the graphitic layers in a BC. Such distance is evaluated by determining the (002) interplanar spacing using the Bragg's equation [69]. Other important structural parameters of the BC are the correlation length along the c-axis (L_c) and the correlation length along the basal plane (L_a), which are evaluated with the Scherrer's equation starting from the (002) and (100) reflections, respectively [70]. Such parameters allow the size determination for the ordered domains in bulk BC and thus gauge whether the BC is amorphous, turbostratic (small size of the ordered domains; it is also known as *"hard carbon"*) or graphitic (large size of the ordered domains) [71]. It was shown that Na^+ uptake in BC anodes is favoured by an amorphous/turbostratic structure due to the more facile accommodation of Na^+ species at the defect sites [72,73]. A preliminary assessment of graphitization of BC could be done through Fourier transformed infrared (FT-IR) spectroscopy aiming at identifying hydrogen-, oxygen- and nitrogen-containing functional groups and providing very useful information concerning the degree of graphitization of the carbon matrix [74–76]. Nevertheless, a significant drawback of BC is related to its great IR absorption that can be limited by using diffuse reflectance infrared Fourier transform spectroscopy (DRIFTS) [77] and attenuated total reflectance (ATR) [78] approaches.

The other relevant properties of BC, such as porosity and specific surface area, will be discussed in the next sections.

2.2. BC post-production modification

Pristine BC could not meet the bulk and surface properties required for the electrochemical applications (*i.e.*, surface area, porosity, chemical functionalities) [18,79]. Accordingly, several chemical and physical procedures could be implemented to tune BC properties acting on the surface and bulk features. In the following sections, the main routes for tailoring BC properties are systematically discussed.

2.2.1. BC surface tailoring

The functionalization of carbonaceous materials is a well-established practice for producing a wide range of tailored materials. Nowadays, surface texturing with nanostructures represents the core productive step for the realization of catalysts [80], absorbers [81] and multifunctional compounds [82,83]. As summarized in Fig. 3, this process is mainly achieved by dispersing inorganic species on the surface, even if carbon-on-carbon decoration could also be performed.

Carbon-on-carbon tailoring is uncommon in BC tailoring as it is more suitable for high-tech materials, such as carbon fibres [84] or graphene [85]. Zhang et al. [86] reported a chemical vapour deposition (CVD) approach for the growth of carbon nanotubes (CNTs) on nut shell derived BC. This study leads the way in using CNTs-modified BC to produce electrodes used for LIBs [87] and supercapacitors [88]. Bartoli et al. [89] reported a solvent mediated process for tailoring the surface of micrometrical BC spheres produced by pyrolysis of cellulose nanocrystals. Authors described a variety of carbon-carbon decorations on BC surfaces ranging from needles to nanospheres.

CVD is also used for the deposition of metal nanostructures onto several different types of matrices, such as polymers [90], CNTs [91] or carbonaceous feedstock [92]. Metal tailoring of BC through CVD is not well-established, and other routes are preferred.

Accordingly, inorganic tailoring of BC has become a well-established procedure for a wide range of applications, ranging from environmental remediation [93] to electrochemistry [94], by using deposition, chemical reduction, calcination and carbothermal reduction approaches.

Simple deposition of inorganic materials represents an affordable way to produce nanostructured electrodes, useful for biosensing [95] and electrochemical storage applications [96]. The main issue of the simple deposition is the lack of uniformity in the coating layer and its instability under working conditions. A calcination process could improve the adhesion of inorganic decoration without forming reduced material, as reported by Zeng et al. [97]. Similarly, carbothermal processes are used to anchor inorganic materials to the BC surface. Contrarily to calcination, carbothermal reduction involves the simultaneous reduction of inorganic precursor and oxidation of BC with a remarkable surface area increment according to the mechanisms summarized by Shen et al. [98]. The main drawback of this approach is the possible alteration of BC morphology, as reported by Tamborrino et al. in the case of sponge-shaped coffee-derived BC and iron salts precursors [99]. Authors showed the disruption of micrometric particles, but this phenomenon was counterbalanced by the formation of well anchored iron nanoparticles covered by a thin layer of iron oxide. Alternatively, chemical reduction is another possibility to tailor the BC surface with

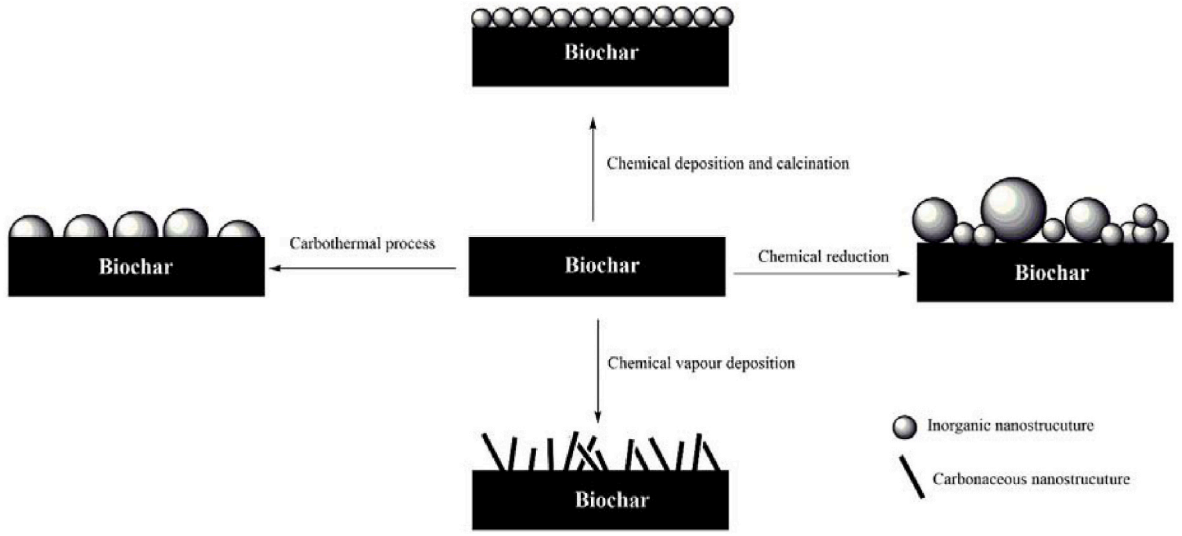

Fig. 3. Summary of surface tailoring routes to produce modified BC.

regular metal-based micrometric and nanosized structures. The reduction process could be performed by using reducing agents such as sodium borohydride [100]. This approach generally leads to an inhomogeneous metal particle size distribution if surfactants are not used as additives [101].

Surface tailoring is not the only modification usually applied to tune the BC properties. The reactivity of BC graphitic-like domains represents a very attractive functionalization route, as summarized in Fig. 4.

Heteroatom doping of BC is achievable by direct conversion of heteroatoms rich feedstock as in the case of N-doping of chitosan derived BC [102]. Doping carbon matrices with nitrogen, sulphur and phosphorous atoms yielding carbon nitride, sulphide, and phosphide functionalities is a well-known approach to modulate their electronic properties, chemical composition, defects, and vacancies [103–105]. The heteroatom functionalization thus acts to modify the surface wettability, electrochemical properties and electronic conductivity of BCs, facilitating the electrode/electrolyte interaction, charge transfer and reaction kinetics [104].

Alternatively, post-production procedures such as ball-milling [106,107], urea impregnation, partial calcination [108], and acid wash could be used [107,108]. Similar approaches could be implemented to introduce P [109], S [110–112] and B [113] sites. BC conjugation with polymeric chains or metal organic frameworks (MOF) is used to both extend the solubility and dispensability range of BC particles and to tailor its chemical properties massively [114,115]. Acidic treatments can introduce a wide variety of oxygen-containing groups, but they will be discussed in the following section, together with the other chemical activation processes.

Evaluation of the effectiveness of the tailoring process is crucial to make operative decisions about the material performances. Several techniques could be efficiently used for determining the functionalization degree. Among them, X-ray photoelectron spectroscopy (XPS) allows to determine the surface chemical composition of the BCs and the chemical states of the different surface elements [116]. XPS is extensively used in the literature specifically to identify the surface functional groups of BCs [70]. It is also used to: (i) gauge the degree of disorder of

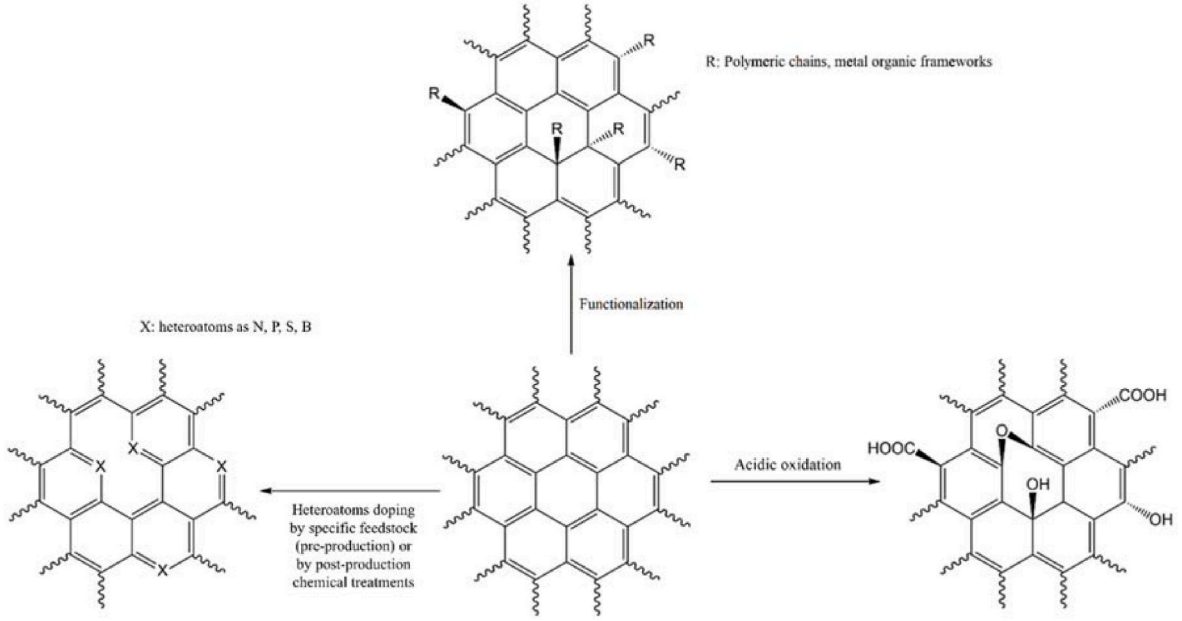

Fig. 4. Summary of some possible functionalization introduced onto sp^2 domains of BC structures.

the carbon surface, being able to discern easily between its various hybridization states [117]; and (ii) detect the impurities (*e.g.*, K, Mg, Cl) on the BC surface, providing a facile avenue to evaluate the quality of the final material [118].

2.2.2. BC activation

Contrarily to surface treatment, activation processes are not used for tailoring the properties of nanostructured carbon materials such as graphene and CNTs but they are largely employed to improve the properties of BC [119] and coal [120]. Activation processes promote a large increment of surface area up to hundreds or thousands of $m^2\ g^{-1}$ [121] through physical or chemical degradation of carbonaceous structures, as discussed in the next sections.

Generally, electrochemical applications require electrode materials endowed with a high specific surface area in order to maximize the charge storage and the effective reaction surface [122]. The specific surface area and porosity (*i.e.*, pore size distribution and pore volume) of BCs, or of any other solid material, can be determined by means of the Brunauer-Emmett-Teller (BET) and Barrett-Joyner-Halenda (BJH) analytical methods. These analyses consist in the adsorption and desorption of nitrogen, whose hysteresis isotherm curve shape is indicative of the type of pores present into the bulk material. Pores are classified on the basis of their diameter: materials can exhibit macropores (diameter >50 nm), mesopores (2–50 nm) and micropores (<2 nm) [123]. Normally, carbon nanomaterials exhibit a BET surface area of 500–1500 $m^2\ g^{-1}$, although functional compounds with 3400 $m^2\ g^{-1}$ of surface area have already been synthesized [124]. In summary, nitrogen adsorption-desorption isotherms are crucial to estimate the porous structures and surface areas of BCs, giving a further tool for the comprehension of their electrochemical activity.

2.2.2.1. Physical treatments. Physical activations are high temperature processes taking place through the reaction of gaseous agent such as CO_2, H_2O or NH_3 with BC matrix at temperature higher than 800 °C [125]. The most diffuse physical activation is based on the use of CO_2 as reported by many authors [125–127] according to the reaction reported in eq. (1).

$$CO_{2(g)} + C_{(g)} \rightarrow 2CO_{(g)} \quad (1)$$

This reaction has a ΔH of 40.79 kcal/mol [128] and promotes a very effective increment of surface area and porosity as reported by many authors [129–131]. CO_2-activation could be also enforced by using not only pure gas but also uncondensable pyrolytic gas and post-combustion fumes.

Alternatively, steam could be used as a replacement for CO_2 induced activation pathway, as reported in equation (2).

$$H_2O_{(g)} + C_{(g)} \rightarrow CO_{(g)} + H_{2(g)} \quad (2)$$

Steam-activation has a lower ΔH of 31.14 kcal/mol [128] compared to CO_2-activation and it promotes not only the increment of surface area but also the removal of tar [132].

Physical activations are simple processes, easily scalable and based on the use of very cheap activation agents but require high energy inputs and long processing times [133].

2.2.2.2. Chemical treatments. Chemical treatments represent the other significant activation processes to increase BCs surface area and porosity. They can be regrouped into three main groups: i) alkaline, ii) acids and iii) oxidants-mediated processes.

Alkaline chemical activations are generally performed by using sodium or potassium hydroxide [134,135] or carbonates [136–138], inducing a complex reactivity as reported in the following equations (3)–(8), where M = Na, K:

$$4MOH_{(s)} + C_{(s)} \rightarrow 4\ M_{(s)} + CO_{2(g)} + 2H_2O_{(g)} \quad (3)$$

$$6MOH_{(s)} + C_{(s)} \rightarrow 2\ M_{(s)} + H_{2(g)} + 2M_2CO_{3(s)} \quad (4)$$

$$M_2CO_{3(s)} \rightarrow M_2O_{(s)} + CO_{2(g)} \quad (5)$$

$$4MOH_{(s)} + C_{(s)} \rightarrow 4\ M_{(s)} + CO_{2(g)} + 2H_2O_{(g)} \quad (6)$$

$$4MOH_{(s)} + 2CO_{2(g)} \rightarrow 4M_2CO_{3(s)} + 2H_2O_{(g)} \quad (7)$$

$$M_2O_{(s)} + H_2O_{(g)} \rightarrow 2MOH_{(s)} \quad (8)$$

BC activation mediated by alkaline media occurs at temperatures higher than 700 °C, but requires significantly less time than physical activation [121] and an acidic wash to remove all the inorganic species remaining after the process. As enlightened by the chemical reaction reported in eqs. (3), (5) and (6), CO_2 and H_2O formed as decomposition products of alkali medium could promote further activation reactions according to eqs. (1) and (2).

Acidic-mediated activation is generally performed using strong oxidant acids such as HNO_3 [139] or H_3PO_4 [140]. This approach requires a low temperature above 80 °C and short reaction times [141], promoting, as shown in Fig. 4, the insertion of oxygenated functionalities on the surface of BC.

The use of oxidant agents such as hypochlorite [142], persulfates [143,144] or hydrogen peroxide [145] promotes an activation process very close to the one achieved by using acidic media.

3. BC as electrode material for sodium ion batteries

3.1. Sodium ion storage mechanism in BC

The anodic behaviour of any material for the NIBs mandatorily requires a lower sodium ions intake and extraction potential compared with metallic sodium. Noticeably, highly ordered graphitic materials could satisfy these condition for lithium but they cannot reach the same performances for sodium [146,147].

As reported by Stevens et al. [148], highly graphitic carbonaceous materials cannot accommodate large amounts of sodium between the graphite layers with an expansion of the interlayer spacing, as in the case of lithium. This is due to the chemical potential of sodium that is lower than the one of the metal itself. Accordingly, metallic sodium is more energetically induced to electroplate on the surface of the carbon surface. An alternative to highly graphitic carbon, disordered carbonaceous materials known as hard carbons are solid alternatives for realizing NIBs. These highly disordered materials contain nanoscale porosity formed by several graphene sheets piled and twisted. In hard carbon, sodium insertion also occurs in the nanopores with an adsorption process with a low voltage plateau in the potential/capacity curve. Authors observed that the sodium species in these pores have a chemical potential close to the metal itself.

Recently, Alvin et al. [149] evaluated the carrier-ion storage mechanism of Li^+, Na^+ and K^+ in hard carbons samples. This study showed improved adsorption of ions on the defective regions and the edges.

Among hard carbons, BC is the most suitable for the development of anodic materials for NIBs. BC presents small and highly disordered graphitic domains, even after annealing up to 1500 °C [36], with micro-porosity that can receive and host Na^+.

Alvin et al. [150] explored the mechanism of sodiation of BC produced from lignin considering the Na^+ uptake on the edges and defect sites, on the interlayer space between graphitic layers and into micropores as reported in Fig. 5.

This process was further studied by Gomez-Martin et al. [151] by investigating the mechanisms responsible for storage in low- and high-potential regions using olive stones-derived BC, produced using a pyrolytic temperature ranging from 800 to 2000 °C as reported in Fig. 6. By means of deep characterization measurements, authors demonstrated that, for the material herein investigated, the sodiation mechanism proceeds through adsorption-intercalation, although

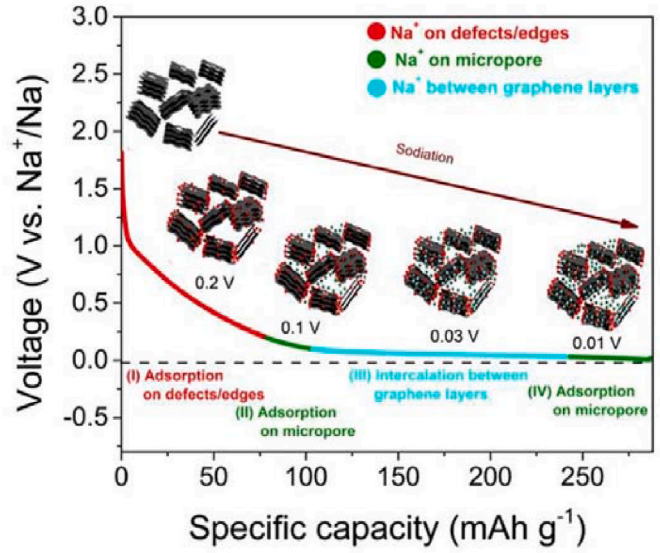

Fig. 5. Sodiation mechanism in lignin derived BC. Reprinted with permission from Ref. [150].

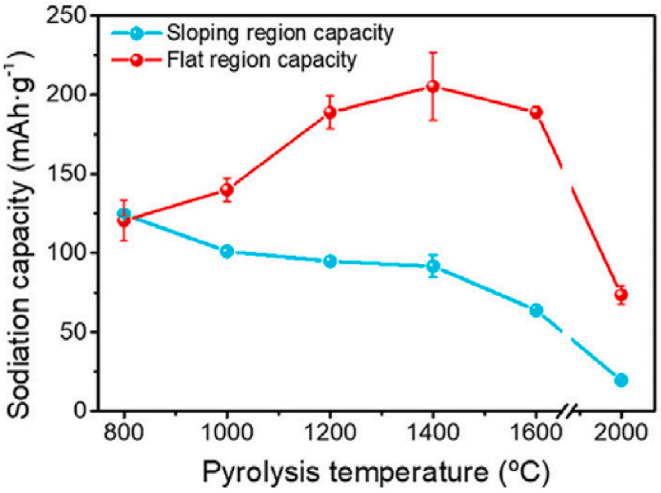

Fig. 6. Sodiation capacity in hard carbons as function of pyrolytic temperature as reported by Gomez-Martin et al. [151] (Copyright © 2019 American Chemical Society).

intercalation-adsorption is also considered and discussed. The correct mechanism assigned is still debated due to the large variety of materials that fall under the simple name of BC. Bommier et al. [152] suggest that insertion into defective sites is more impacting on the sodiation than the intercalation process. Some key points remain valid for any material studied, such as a positive correlation between the decrement of sloping capacity with increment of long- and short-range order of BC structure.

Raman spectroscopy, which probes material properties on a shorter-range scale than XRD, could be performed on hard carbon-based electrodes to monitor the structural changes induced in the host matrix by sodiation/desodiation [63] and, more generally, by insertion/extraction of alkali metal ions [153]. Raman scattering can be measured after or before pulling out the electrode material from the electrochemical cell (*ex-situ* and *in-situ* measurements, respectively). The former measurements allow easily evaluating the reversibility of the Na^+ (Li^+/K^+) ion storage, even if some caution is needed as sodium deintercalates in air [63]. Different from *ex-situ* analysis, *in-situ* measurements require the use of special cells equipped with optical windows. By appropriately setting the measurements conditions, *in-situ* analysis can also be carried out during the electrochemical reaction (in *operando* conditions) to clarify the sodiation mechanism [63,153,154].

The storage mechanism of sodium in hard carbons has not been fully understood and is still a matter of debate. As comprehensively reviewed by Sun et al. [155], several models (such as "insertion-filling", "adsorption-filling", "adsorption-insertion", and "multistage mechanism") try to explain, through complementary analysis techniques, the sodiation process on the basis of the structural changes evidenced in relation to the microstructure of the host material. The Na^+ ion storage in hard carbons involves a combination of edge/defect sites and progresses through adsorption, intercalation and pore-filling, similar to the Li^+ ion storage [62,63].

As mentioned above, the charge/discharge curves of hard carbon-based anodes in both LIBs and NIBs are featured by a high-voltage sloping region, generally followed by a low-voltage plateau [155]. The former region is often associated with the sodium/lithium intercalation between the disordered layers of the turbostratic nanodomains, while the discharge capacity in the plateau region is ascribed to the occupation of macropores between turbostratic nanodomains and adsorption into nanopores [53,63,153,156]. The complementary picture has also been proposed, indicating the storage of Na^+ ions in the edges/defects/surface of hard carbons and the turbostratic nanodomain interlayers associated with sloping and plateau regions, respectively [54,154,157].

Only a few studies report *in-situ* RS analysis under *operando* conditions of hard carbon-based NIB electrodes. These studies have evidenced that a downshift of the G-band accompanies the increase of capacity in the high-voltage sloping region, while the D-band remains at constant frequency, progressively weakening until it disappears. No further changes in the G-band frequency and D-band intensity are observed in correspondence with the increase of capacity in the plateau region [63,153]. According to the authors, since the frequency of the G-band is sensitive to the C–C bonding strength, which changes due to the charge transfer from the alkali metal atoms to π^* antibonding orbitals of the carbon matrix, its downshift is related to the intercalation process. As the frequency of the G-band no longer varies, as observed in both LIBs and NIBs in the plateau region, no further ions are intercalated. Thus, the downshift gives a measure of the amount of intercalated alkali metal ions, with the different intercalation limits for Li and Na resulting in different minimum frequencies of the G–band. In a simplified picture, an increasing content of alkali metals causes the Fermi level to continuously upshift due to the electron transfer, and the available free states in the conduction band progressively decrease until they are missing. Since the double-resonance process behind the detection of the D-band requires the availability of empty states in the band structure near the Γ-point above the Fermi level, this ultimately leads to the disappearance of the band. Thus, the plateau region capacity is attributed to the pores' surface adsorption and the formation of metal clusters inside them [62].

X-ray absorption spectroscopy (XAS) is able to provide information on the oxidation state, atomic proximity structure, coordination number and bond length of the atoms included in the bulk of a sample [158,159]. For these reasons, it proved to be useful in studying the processes of sodiation and desodiation at the anode of sodium batteries. A significant drawback of this family of analytical techniques is that it is very challenging to directly probe elements whose atomic number is lower than ca. 20, thus excluding Na and C [160]. Hence, the applicability of XAS techniques is typically limited to anode materials wherein Na species are reversibly stored in phases based on other elements such as Ti [161], Cu [162], Mo [162] and P [163,164]. Though such anode materials often include a carbonaceous matrix, the latter is introduced mainly to raise the electrical conductivity and not to reverse store Na species. Thus, in most of these anode materials, the carbonaceous matrix does not need the rich morphology and porosity that are bestowed by BCs. Accordingly, conventional artificial carbons are adopted in the synthetic processes (*e.g.*, graphite powder [164], Super C65 carbon [161], reduced graphene oxide [162] or Ketjen black [163]).

Mössbauer spectroscopy is typically used to probe the chemical state of atoms such as Fe [165], Sn [166] and Sb [167], that are often used in carbon-based materials meant for application at the electrodes of electrochemical energy conversion and storage devices [168,169]. This is particularly relevant if we consider that Sn and Sb are attractive anode materials for NIBs due to their remarkable theoretical storage capacities, equal to 847 and 660 mAh g^{-1} [170], respectively. To understand the sodiation/desodiation mechanism of materials based on Sn and Sb is of paramount importance to design anodes exhibiting a maximized capacity and good cyclability [167]. Fe-based anodes for NIBs have also been demonstrated and studied with Mössbauer spectroscopy [171]. The literature reports BC anodes, including Sn species [172]. However, such studies are more concerned with elucidating the feasibility of the anodes for application in a NIB rather than with investigating the fundamental sodiation/desodiation mechanism of the Sn species. In addition, Mössbauer spectroscopy is of little use for conventional BC anodes for NIBs that do not include Sn, Sb and Fe since C is not suitable for the technique [173]. On these bases, the full potential of the Mössbauer spectroscopy in the study of BC anodes for NIBs is still to be explored.

Electron paramagnetic resonance (EPR) is an attractive technique for studying BC anodes because it can detect unpaired electrons found in sodium and carbon species [174,175]. Specifically, it is used effectively to study the BC sodiation/desodiation mechanism upon cycling. Na becomes more metallic at the plateau region due to Na intercalation and filling to form clusters, while it is typically ionic at the sloping region [176]. In addition, the metallic sodium clusters are in the quasi-liquid state at room temperature. Pristine BCs typically do not exhibit EPR signals due to the lack of carbon-centered free radicals and delocalized electrons [176,177]. However, upon sodiation EPR signals appear, ascribed to SEI films [178] and the formation of metallic bonds similarly to LIBs [179]. EPR is particularly suitable also for detecting localized paramagnetic centers associated with different aromatic π radicals on carbon [180]. Such species are strongly affected by the dangling bonds on the carbons [181], which are modulated by the carbon structure and, ultimately, by the pyrolysis temperature. At low pyrolysis temperatures, characteristic localized spin centers are revealed, assigned to dangling σ bonds at sp^2 carbon edges or on open micropores [182]. As the pyrolysis temperature is higher: (i) signals with broad peaks are detected, indicating the presence of conduction carriers; and (ii) it is revealed that few dangling bonds able to react with oxygen are present [183].

Also, electrochemical tools such as Electrochemical Impedance Spectroscopy (EIS) are powerful in determining several relevant features including: (i) the overall ohmic resistance; (ii) the diffusion migration resistance (R_{SEI}) of sodium ions through the SEI film; (iii) the charge transfer resistance (R_{ct}); (iv) the Warburg impedance (Z_W) associated with the diffusion process of sodium ions inside the material; and (v) the capacitance arising from both the passivation film and the electric double layer capacitor [184]. All these parameters can be determined under *operando* conditions on a fully assembled cell along the charge/-discharge process, providing crucial information on the evolution of the anode of the sodium battery upon cycling as the polarization potential is varied [185]. In particular, the diffusion coefficient of sodium in carbon changes between the slope zone and the plateau, indicating a change in the binding energy and a reversible structural phase transition [186,187]. EIS is also very useful for studying the evolution of the SEI, with a particular reference to its ionic conductivity [174]. EIS parameters determined as a function of the temperature can elucidate the dynamic properties of the resistance and the activation energies for the individual processes or components in the sodium battery. A typical example is the study of the diffusion of sodium ions through the SEI and how the latter phenomenon is affected by the different features of the cell (*e.g.*, the composition of the electrolyte) [188]. A much more detailed picture of the electrical features and of the mechanisms associated with long-range charge transport phenomena can be obtained by broadband electrical spectroscopy (BES) [189–192]. This technique investigates at a high level of detail the electric response of a sample as a function of the frequency of an applied electric field and of the temperature [193]. BES allows for the fine elucidation of the polarization and relaxation phenomena occurring within a material, that are associated with: (i) the mesoscale structure, with a particular reference to the segregation in domains with different permittivity; and (ii) the dynamics of the functional groups found within the system. By integrating this information with the outcome of other complimentary techniques (*e.g.*, thermoanalytical analyses carried out by MDSC and DMA [194]; vibrational spectroscopies [195]) it becomes possible to identify the charge percolation pathways and how they are correlated to the composition and physicochemical features of the material. Traditionally, BES has been widely applied to study ion-conducting and cathode materials [196–198]. Very recently, the BES technique has been applied to study the interactions between carbon matrices and electrode materials for battery applications [199]. Specifically, the carbon phase has a primary role in determining the mobility of Li^+ ions in the electroactive material (*e.g.,* $LiCoO_2$) [199]. Though in principle, it is feasible to use BES to investigate battery anodes (*e.g.*, to study intercalation/de-intercalation mechanisms or the features of the SEI), in practice, as of today, very little work has been done in this area. Nevertheless, this leaves the potential of BES to investigate the anodes of sodium batteries based on BCs largely unfulfilled.

Computational modelling can be used to interpret and predict the structure and electrochemical properties of electrode materials for rechargeable batteries, with first-principles density functional theory (DFT) being nowadays the most widely used approach [200,201]. In this regard, the electrochemical intercalation of alkali metals in disordered hard carbons or nanoporous carbons remains challenging, mainly due to the structural complexity involved. The structural features of hard carbons, especially the BC produced from biomass, depend on the matrix and the preparation route, and may not be comprehensively captured in simplified models suitable to investigate intercalation phenomena at the atomic scale. The identification of the active sites for the alkali metal uptake needs to be addressed by investigating the structure of hard carbons. Hard carbons typically contain numerous defect sites originating from residual heteroatoms (*i.e.*, hydrogen, oxygen, nitrogen, inorganics), carbon vacancies formed during the heat treatment, and different arrangements of graphitic domains in an otherwise disordered carbon matrix. Thus, the clear relation between structure and electrochemistry behaviour and the dominating mechanisms at the atomic scale for alkali metal insertion/extraction in these systems remains controversial. As already discussed in this section, several interesting alternative mechanisms have been proposed, based on experimental evidence, to interpret the electrochemical structure−property relationships of hard carbon [148,202], including the "intercalation–adsorption" mechanism, also known as "house of card" model [148], and more recent works that assigned the high-potential sloping region to ion adsorption instead on the defect/edge sites, and the low-potential plateau to ion intercalation into the graphitic layers [203].

Due to this uncertainty, which is critical to be solved to direct the preparation of hard carbons towards optimized microstructures for alkali-ion storage, significant efforts have been devoted in recent years to rationalising the experimental voltage profile from a computational perspective. The main techniques used to this end are DFT-based energy minimization and reactive force field (ReaxFF) molecular dynamics (MD), also in association with Monte Carlo simulations, in the so-called hybrid grand canonical Monte Carlo/MD (GCMC/MD) method [204].

Through computational modelling it is possible to evaluate the feasibility of Na ion intercalation at specific sites by calculating the sodium binding energy according to the following equation (9):

$$E_b = \frac{E_{Bulk+xNa} - E_{Bulk} - x_{Na}E_{Na}}{x_{Na}} \quad (9)$$

where $E_{Bulk\ +\ xNa}$ is the total energy of the systems with x_{Na} added Na

species, E_{Bulk} is the total energy of the systems without Na, x_{Na} is the number of added Na, and E_{Na} is the total energy of one ionic sodium. A positive E_b would indicate that intercalation or storage in the specific system is energetically unfavourable.

Voltage profiles, for various model structures, are determined in computational studies from the calculated formation energies of intercalated Na_xC compositions and Na metal (Na_{bcc}), following equation (10):

$$V(x_2, x_1) = \frac{E(Na_{x2}C_y) - [E(Na_{x1}C_y) + E(Na_{bcc})]}{-zF(x_2 - x_1)} \quad (10)$$

where E ($Na_{x1}C_y$) and E ($Na_{x2}C_y$) correspond to the formation energies of two structures that differ by the number of Na atoms under a fixed number of carbons, and E (Na_{bcc}) is the total energy of metal sodium; F denotes the Faraday constant, z is the number of electrons per Na atom involved in the reaction, and V represent the open-circuit voltage.

While the application of eq. (9) and eq. (10) is straightforward, the real difficulty in these calculations is the accuracy in the calculation of the formation energies of intercalated compositions, which strongly depends on the structural model assumed, as well as on the accuracy of the underlying computational approach. DFT-based simulations are expected to give greater accuracy in the calculation of properties related to the electronic structure of HC materials but, due to their computational cost, are limited to relatively small-size models (*i.e.*, 50 atoms [203]), that selectively represent specific structural or defect aspects (*e.g.*, presence of vacancies or oxygen atoms) and the insertion of a very limited number of alkali ions [149,202,205–207]. ReaxFF-MD simulations are critical to catch the structural disorder over longer scales, as simulation models can include several thousands of species, thus providing the opportunity to construct models that represent the experimentally observed complex structural features of these systems, including at the same time carbon layers with continuous and irregular curved moieties, different sheet orientation, stack distribution, pore connection, extended defects such as stacking faults and dislocation, expanded layer spacing in graphitic-like domains [208–210].

Energy minimization techniques based on first principle DFT approach have clarified, for example, the reasons behind the different Li/Na/K storage mechanisms of hard carbon anodes, determined by different atomic interactions between the alkali metal and the carbon matrix [206] in graphite-like layers, revealing that much less electrons of Na are transferred in this process compared to Li and K, which indicates the strong Li–C and K–C interactions and a weaker Na–C interaction. In addition, it was found that defects on the carbon layers may have an impact on the atomic interactions including the metal–metal and metal–carbon interactions, thereby determining whether the stored alkali-metal atoms are in ionic or quasi-metallic states.

The application of a combined experimental/computation approach based on DFT modelling of HC supported the proposition of a revised mechanisms of intercalation for Na ions in which the alkali ions are initially bonded simultaneously and continuously at defects, within interlayers and on pore surfaces; subsequently, at higher sodiation level, when such higher energy binding sites are filled, pores filling occurs during the plateau region, where the densely confined sodium takes on a greater degree of metallicity. Based on the structural models investigated, the effect of defects was analysed, suggesting that different defect types influence the energetics of sodium storage differently, both at the defect site and at the nearest sites. In particular, oxygen defects in the graphitic layers were shown to promote stronger sodium adsorption energies, especially at low sodium loading, which could contribute to the irreversible capacity observed in the first cycle, with sodium remaining trapped at these sites [207].

DFT-based simulations are also used to guide the interpretation of experimental data different from the voltage-capacity profile, such as Raman spectra. For example, using simplified models of graphene layers with AA stacking, the gradual shift of the Raman G-band along with the Na amount inserted between the layers was calculated, in agreement with experiments, while it was suggested that the presence of defects hardly influences the band structure and phonon dispersion. On the contrary, the effect of defects was shown to be significant on the energetics of the systems in terms of voltage profile curves and, in particular, Na diffusion as, for example, migration barriers for Na ions close to defect sites are higher than in regular sites [203].

ReaxFF-MD results can be directly correlated to experimental structural features, such as the interlayer distances, as derived from XRD, the atomic percentages of different carbon components, in terms of *sp*, sp^2 or sp^3 hybridization, as derived from XPS analysis, and the pair distribution functions (PDFs) to obtain information on the local carbon structure. Such valuable information can not only be used to guide the interpretation of the experimental data but also to assess the validity of the structural model in representing the real structural complexity of the system [208]. Such an assessment is crucial to support the computational findings related to the intercalation mechanism, as this depends on the HC structure. In particular, based on ReaxFF-MD simulation, the voltage profile curve of HC was interpreted as a three-step process starting with chemisorption on the surface active sites of the graphite sheets, where defects (*e.g.*, non-hexagonal rings) are expected to increase the capacity by promoting the formation of small sodium clusters, followed by intercalation between the carbon layers with suitable d-spacing and, as a final stage, nanopore filling and metal sodium clustering formation.

Few studies explicitly address the computational investigation of biomass-derived HC. In this regard, MD simulations were used, for example, to investigate the alkali ion binding mechanisms and diffusion rates in lignin-based hard carbon models differing by the crystalline volume fraction (CVF) [210]. The hard carbon models were constructed to reproduce the nanostructure of hardwood lignin pyrolyzed and reduced at 1000, 1500, and 2000 °C as synthesized and characterized by Tenhaeff et al. [211]. Those models included very high numbers of C species (100000–700000 atoms), necessary to capture both the mesoscale structure of lignin-based carbon composite anodes and an accurate CVF with appropriately sized crystallites. Calculation of the binding energy distribution of alkali ions within the C matrix suggests which intercalation positions are more energetically favourable for lithium and sodium, respectively. At the same time, MD simulations are suitable for deriving diffusion coefficients for the alkali ions in these systems and, consequently, migration barriers for alkali-ion intercalation. Analysis of the results supported a likely intercalation mechanism following the scheme adsorption–intercalation-pore filling upon sodiation and suggested that lignin-based hard carbons with lower CVF, smaller nanocrystallites, and moderate porosity would allow for the highest energy density for sodiated anodes.

The application of computational-based approaches provides guidance rules to design optimized biomass-derived HC anode materials, notwithstanding the complexity of these systems.

3.2. Use of neat BC as anode material for NIBs

The first Na-ion cell with BC was assembled in 1993 by Doeff et al. [212], who demonstrated that petroleum coke successfully undergoes reversible insertion of sodium ions and can thus be used in rechargeable NIBs as summarized in Table 2.

The use of simple biomolecules such as sugars has been an interesting test bench for the production of hard carbon with tuneable morphologies. As reported by Yamamoto et al. [213], several sugars (*e.g.*, glucose, sucrose, maltose) and sugars based polymers (*e.g.*, cellulose,

Table 2
Overview of neat BC used for the production of NIBs anode materials.

Feedstock	Pyrolysis conditions		Specific Surface Area ($m^2 g^{-1}$)	d spacing (nm)	Highest capacity (mA g^{-1})	Current density (mA g^{-1})	ref.
	Optimal temperature (°C)	Time (h)					
Lignin	1300	6	48.3	0.375	183	300	[150]
Olive stones	1400	1	4.1	0.38	291	20	[151]
Saccharides	1300	1	506	0.389	353	25	[213]
Sucrose	1600	2	n.a.	n.a.	270	6000	[51]
Cellulose	1600	1	5	n.a.	310	37	[214]
Banana peels	1100	5	130.8	0.376	355	50	[215]
Coconut shells	1300	1	9	0.391	270	50	[216]
Corn silk	1300	1	6	0.375	273	50	[216]
Walnut shells	1300	1	11	0.368	293	50	[216]
Peat moss	1100	1	196.6	0.37	298	50	[217]
Peanut skin	800	1	1930	0.388	431	100	[218]
Wood	1000	2	n.a.	n.a.	275	10	[219]
Lychee seeds	500	2	6.61	0.37	225	200	[220]
Apple pomace	600	1	117.3	n.a.	255	50	[221]
Apple pomace	600	1	117.3	n.a.	86	5000	[221]
Pine pollen	900	1	171.5	n.a.	201	100	[222]
Hemp haulm	600	3	n.a.	n.a.	256	37.5	[223]
Dandelion	1200	5	4.7	0.37	372	50	[224]
Date palm	1400	1	34.7	0.37	300	25	[225]
Switchgrass	1000	2	619.8	0.376	225	50	[226]
Switchgrass	2050	2	23.1	0.376	110	5000	[226]
Resinous pine wood	1400	1	45	0.381	310	33	[227]
Cellulose nanofibers	1000	2	377	n.a.	255	40	[228]
Bamboo	1000	1	29.1	0.39	320	50	[229]
Cellulose nanocrystals	1000	2	145.6	0.39	340	100	[230]
Lignin/PAN composite	1300	0.5	27	0.373	293	20	[231]
Corn stalks	1000	2	9.24	0.4	270	60	[232]
Maize husks	1100	2	267.7	0.48	255	50	[233]
Reed straw	1300	3	36.2	n.a.	372	25	[234]
Rice husk	1300	2	2.7	0.395	372	25	[235]
Loofah sponge	800	1	n.a.	n.a.	390	25	[236]
Mushroom spores	1400	1	14.7	0.371	303	20	[237]
Argan shells	1200	1	8.6	0.393	333	25	[238]
Peanut shells	600	5	375.2	n.a.	193	250	[239]
Rape seed shucks	700	2	11.9	0.39	196	25	[240]
Rape seed shucks	700	2	11.9	0.39	62	2000	[240]
Lotus stems	1400	1	24.4	0.368	250	100	[241]
Phoenix tree leaves	700	2	1824	0.388	134	100	[242]
Waste tea bag powder	1000	2	521	0.384	193	100	[243]
Waste tea bag powder	1000	2	521	0.384	127	1000	[243]
Algal blooms	1000	5	n.a.	0.365	230	20	[244]
Coffee ground	970	6	787	0.386	173	60	[245]

glycogen, amylopectin) displayed high reversible sodiation capacity, especially thanks to a crucial pyrolytic step at 275 °C that stabilizes the carbonaceous structures.

3.2.1. *The influence of BC structure on the electrode performances*

Li et al. [51] used sucrose for the production of sub-micrometric BC spheres (with an average size of about 300 nm) through a combination of hydrothermal and pyrolytic processes with temperatures ranging from 1000 up to 1600 °C. The authors covered the hard carbons with a layer of highly graphitic carbon by mixing the inert carrier gas with toluene vapours. As reported, the initial Coulombic efficiency (CE) of BC spheres reached the 83 % and plateau capacity at the low potential region increased with increasing pyrolysis temperature. Accordingly, the BC produced at 1600 °C showed a plateau capacity of 220 mAh g^{-1} together with a high cyclability achieving capacity retention of up to 93 % after 100 cycles. The authors also reported full cell characterization using air-stable P2–$Na_{2/3}Ni_{1/3}Mn_{2/3}O_2$ as a cathode, achieving an energy density of 200 Wh kg^{-1} with an initial CE of 76 %.

Similarly, Simone et al. [214] pyrolyzed cellulose in a temperature range from 700 up to 1600 °C observing a largely graphitic formation for temperatures up to 1150 °C. As shown in Fig. 7, the authors observed an increment of the plateau and total reversible capacity together with a

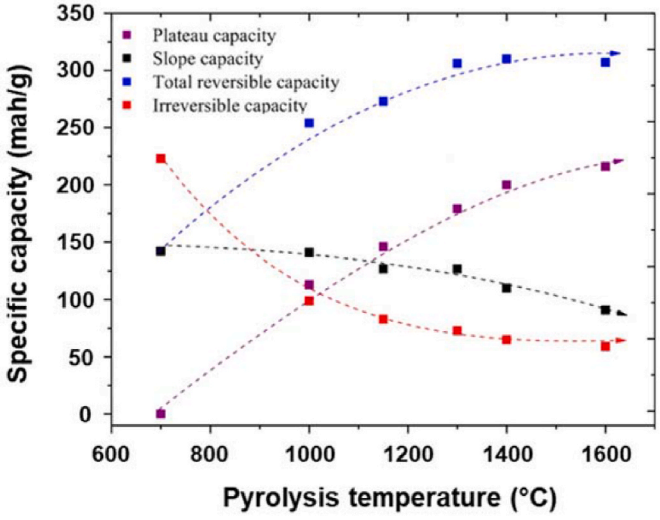

Fig. 7. Capacity trends as function of pyrolytic temperature. Reprint with all permission from Simone et al. [214].

decrement of slope and irreversible capacity by increasing the pyrolysis temperature.

Authors suggested that this behaviour was due to a combination of the simultaneous decrement of specific surface area, increment of micropore size and reduction of graphitic plane spacing.

Lotfabad et al. [215] obtained BC converting banana peels reaching a volumetric capacity of about 700 mAh cm^{-3} even with a limited surface area ranging from 19 to 217 $m^2 g^{-1}$. Nevertheless, the electrodes showed a charge capacity of 221 mAh g^{-1} at 500 mA g^{-1} with a degradation of only 7 % after 600 cycles; lower current density (100 mA g^{-1}) resulted in a higher capacity (336 mAh g^{-1}), but with a more pronounced degradation (by 11 % after just 300 cycles). Similar values were achieved by Nita et al. [216] by BC derived from coconut shells, walnut shells, and corn silk, all of them with a specific surface area of about 10 $m^2 g^{-1}$, achieving reversible capacities of around 300 mAh g^{-1} at a current density of 50 mA g^{-1}. Among them, the highest capacity (293 mAh g^{-1}) and the highest capacity retention (93 % of the initial capacity after 100 charge/discharge cycles) were reached using walnut shells-derived BC. Authors suggested that the adsorption-insertion mechanism of sodium storage could be associated with the optimal interlayer space and the presence of defective graphene layers.

Morphological properties of BC are crucial in the activity of BC as anodic material, even more than surface area. Ding et al. [217] converted peat moss into a hierarchical BC with both micro- and meso-porosity in the shape of nanosheets. The porous distribution accounted for the high-rate performance, due to the good accessibility by the electrolyte and the reduced diffusion distances for sodium ions. The authors claimed a very stable cycling capacity of about 298 mAh g^{-1} at a current density of 50 mA g^{-1}, with a CE close to 100 % and a negligible voltage hysteresis. Similar results were achieved by producing microporous [218] or mesoporous BC [219,220]. Interestingly, macro-porous materials could also display a remarkably high efficiency. For instance, Fu et al. [221] produced a macro-porous BC (with some tiny pores inside the macropores) derived from apple pomaces, achieving a capacity of 208 mAh g^{-1} with a CE of around 99 %. Authors suggested that such a hierarchical 3D structure of BC could provide the microspaces for sodium storage and dissipate the volumetric expansion.

Interconnected 3D networks play a relevant role in BC behaviour in sodium batteries. Zhang et al. [222] produced a honeycomb-structured BC derived from pine pollen, achieving a capacity of 370 mAh g^{-1} at a current density of 0.1 A g^{-1} (the system retained a reversible capacity of 203 mAh g^{-1} after 200 cycles). The authors suggested that the behaviour was due to the large layer spacing among graphitic domains (up to 0.41 nm), favouring sodium ions to intercalation/deintercalation.

Wang et al. [223] moved a step forward and suggested that also the appropriated surface texture could enhance the capacity with an appreciable increment of sodium ions insertion.

Not only the spatial arrangement of the graphitic domains affects the electrode properties, but also the graphitic domains themselves, as proved by Wang et al. [224]. The authors produced dandelion-derived BC using pyrolytic temperatures ranging from 800 to 1400 °C, thus increasing the crystallite volume from 60 to 210 nm^3. The pyrolytic temperature increase significantly raised the plateau capacity below 0.1 V. However, it did not affect the sloping capacity above 0.1 V, suggesting a strong relationship between the amount of sodium ions deintercalation and the dimension of pseudo-graphitic domains. Similar results were achieved by Izanzar et al. [225] by using date palm waste. Noticeably, BC is a non-graphitizable carbon [36,246,247], so the enlargement of graphitic crystallites is limited in space [42], even at high temperatures. Zhang et al. [226] annealed switchgrass derived BC at 2050 °C, enlightening interesting features compared with non-annealed BC. Authors reported comparable specific capacities for all pristine and thermally annealed BC by using current density in the range from 0.05 up to 0.1 A g^{-1}, but they pointed out a lower capacity decay for the annealed samples at higher current density (in the range between 0.5 and 5 A g^{-1}). Annealed BC showed impressive stability with capacity retention of up to 87 % over 800 cycles and CE close to 100 %. A very deep insight into the sodium behaviour in BC treated at such high temperatures was reported by Morita et al. [248] by using ^{23}Na-NMR. Authors strongly correlated the size of sodium clusters with the temperature of the annealing process, proving that 2000 °C induced the formation of clusters with a quasi-metallic behaviour.

3.2.2. *BC electrodes from different feedstocks*

The correlation between BC feedstock and its electrochemical performance is complex. Saavedra Rios et al. [249] reported a systematic overview of different feedstocks, such as pine, ash, wheat straw and miscanthus, subjected to the same pyrolytic process at 1400 °C. The uncontrolled complexity of the pyrolytic process and the high heterogeneity of the feedstocks in terms of chemical and morphological properties did not allow the definition of a univocal correlation between the used feedstock and the performances of the corresponding electrode. Nevertheless, the authors established a correlation between lignin, hemicellulose and inorganic contents and BC performances, albeit still not fully exhaustive. The study suggested using pure lignocellulosic biomasses BC as a benchmark to evaluate the electrochemical behaviour of the various systems.

Luo et al. [228] used cellulose nanofibers to produce a long-life anode used in rechargeable NIBs. The authors pyrolyzed the feedstock at 1000 °C for 2 h, achieving a reversible capacity of 255 mAh g^{-1} at a current density of 40 mA $g^{-1}$and 85 mAh g^{-1} at 2000 mA g^{-1}. The authors observed high cycling stability, with 180 mAh g^{-1} capacity, even after 600 cycles at 200 mA g^{-1}. Similarly, Zhang et al. [229] produced micrometric tubular structures with various lengths but an inner diameter of around 30 nm, reaching a reversible 320 mAh g^{-1} capacity at 5 mA g^{-1}. Alternatively, Zhu et al. [230] pyrolyzed cellulose nanocrystals at 1000 °C, producing a porous BC, obtaining a reversible capacity of 340 mAh g^{-1} at a current density of 100 mA g^{-1}.

Jin et al. [231] used lignin to produce nanofibrous BC through a co-pyrolytic process with polyacrylonitrile at temperatures ranging from 800 to 1300 °C. The self-standing, binder-free electrode showed a reversible capacity of 293 mAh g^{-1} at a constant current density of 20 mA g^{-1}, with an initial CE of 71 %.

Pure lignocellulosic components could be used to produce a wide variety of BC architectures. However, their isolation from biomasses requires multistep processes that make them not so appealing; as a matter of fact, lignocellulose is usually used as a whole for the production of anode material. One of the most abundant and economically convenient sources of lignocellulose is crop-derived biomass, even if its use represents an ethical issue due to food destination [250]. Many studies have exploited the use of crop residues and derivatives as the source for the production of BC to be used in energy devices. Cong et al. [232] hydrothermally treated corn stalks, simultaneously carbonizing the biomass and removing the inorganic components. The so-obtained material was used without further treatments as an anode material, with a reversible capacity of 270 mAh g^{-1} at 0.2C and 172 mAh g^{-1} at 10C (the capacity was remarkably maintained up to 97 % of the initial one even after 100 cycles).

Yang et al. [233] studied BC obtained from pyrolyzed maize at different temperatures from 500 up to 1100 °C. BC produced at 500 °C did not display any electrochemical activity, while the other samples were conductive enough to be used as electrode material. Authors reported the best performances using BC produced at 1100 °C, achieving a reversible 240 mAh g^{-1} capacity. Also, rice derived waste-streams [234,235] and old loofah sponges [236] are good choices to produce anode for NIBs, with specific capacities above 350 mAh g^{-1} at 25 mA g^{-1}current density.

Several other neat lignocellulosic biomasses (*i.e.*, mushroom spores [237], argan shells [238], peat moss [217], peanut shell [239], rape seed shuck [240], lotus [241], leaves [236,242]) have been used to produce BC for NIBs applications. However, using biomass waste-streams represents a very interesting route to improve the BC-based electrodes

sustainability. Arie et al. [243] used waste tea bags derived BC as feedstock for a hydrothermal/pyrolytic conversion route producing NIBs anodes with an initial capacity of 375 mAh g^{-1} at a current density of 100 mA g^{-1}, maintaining a capacity of 193 mAh g^{-1} after 100 cycles.

Another interesting approach is based on the conversion of harmful biomasses, such as those recovered from algal blooms, as reported by Meng et al. [244]. The authors pyrolyzed the feedstock in a temperature range from 700 up to 1000 °C, achieving a specific capacity of 230 mAh g^{-1} at a current density of 20 mA g^{-1}.

3.3. Use of engineered BC as anode materials for NIBs

Tailoring the chemical properties of BC (by following some of the strategies described in Section 2.2) is a key issue for adjusting its performances as an anode material, as overviewed in Table 3.

A first feasible approach is the pre-treatment of the feedstock to remove the inorganic content. Beda et al. [269] studied three different cellulose-rich biomasses (*i.e.*, asparagus, potato and grape waste), either washing the biomass with water at 60 °C before the pyrolysis or washing the pyrolyzed BC with hydrochloric acid at room temperature. These two gentle wash procedures reduced the inorganic content of about 10 wt% on the final BC (with respect to the BC obtained without any washing treatment). Interestingly, the BC produced by both routes showed slightly higher surface area values than non-treated BC, in the 50 m^2 g^{-1} range. Nevertheless, the electrochemical capacity of the washed materials is not significantly higher than the capacity of non-washed BC (only when the washing step is carried out before the pyrolysis, the capacity is slightly higher). Susanti et al. achieved a more effective demineralization using hydrochloric acid on BC at 60 °C for 24 h [270]. The resulting BC showed improved performances compared to the neat one, showing high capacity at a current density of 50 mA g^{-1} (up to 317 mAh g^{-1} at the beginning, with a plateau capacity at 244 mAh g^{-1} after several cycles). Interestingly, the authors reported that the demineralization of the feedstock with potassium hydroxide before the pyrolysis, instead, does not significantly affect the electrochemical activity of the material. These observations suggested that pre-treatments induced different reorganizations of the biomass before the pyrolytic conversions, acting not only on inorganic content but also on organic components. This emerged from the work of Dou et al. [271], which proved the detrimental effect of strong and prolonged acidic pre-treatment on the electrochemical performances of the resulting BC. On the other hand, Feng et al. [272] proved that a controlled pre-hydrolytic step mediated by enzymes could boost the properties of the produced BC: indeed, the removal of hemicellulose component increased the amount of pseudo-graphitic domains with a great interlayer spacing, appreciably improving the specific capacity.

Acid treatments could also be used to functionalize and activate the BC. Hong et al. reported that a biomass pre-treatment with phosphoric acid could lead to a very high surface area BC (up to 1272 m^2 g^{-1}), functionalized with phosphoric residues [273]. This material showed a capacity of 181 mAh g^{-1} at a current density of 200 mA g^{-1} (even after 200 cycles), but a very poor CE of about 27 % was obtained due to the formation of SEI induced by phosphorus residues.

Another route for chemical activation was studied by Li et al. [274] by using potassium hydroxide on a cucumber stem-derived BC. The authors followed a two-step process, starting with the pyrolysis at 1000 °C followed by a hydrothermal activation step at 150 °C with a water solution of KOH. Activated BC showed an improvement in the reversible capacity by 36 % with respect to the pristine one.

Another non-acid chemical activation route was reported by Sahu et al. [275] using calcium hypochlorite and activation temperatures ranging from 400 to 900 °C, producing the materials shown in Fig. 8.

The partial oxidation promoted by $Ca(ClO)_2$ induced the conversion of the more amorphous domains of BC into carbon dioxide (in the same way as many other common oxidant agents, such as nitric acid). The *in situ* released carbon dioxide could also act as an activation agent itself, as mentioned in the previous section. The activated BC shown in Fig. 8 presents a lamellae-like surface, with the simultaneous disappearance of the micrometric porosity. Authors suggested without reporting any electrochemical test that the high porous volume (up to 0.141 g cm^{-3}) together with the improvement of graphitization and surface area, could make this BC suitable for sodium ions storage.

Very recently, also Simões dos Reis et al. demonstrated the importance of increasing the porosity to increase the capacity: by treating BC with $ZnCl_2$, they induced the formation of ordered mesopores almost doubling the specific capacity with respect to the untreated material [276].

The activation process acts not merely on surface area and porous

Table 3
Overview of engineered BC used for the production of NIBs anode materials.

Biomass feedstock	Functionality insert	Tailoring reactant	Surface Area (m^2 g^{-1})	Specific capacity (mAh g^{-1})	Capacity of not doped BC (mAh g^{-1})	Current density (mA g^{-1})	ref.
Wood powder	C=O	Tetramethoxysilane	n.a.	330	190	40	[251]
Grapefruit peels	N	Melamine, urea and citric acid	10	187	110	37	[252]
Cellulose	N	Chitosan	n.a.	395	278	100	[253]
Okara from soybean	N	Main feedstock	n.a.	292	/	56	[254]
Honey	N	Main feedstock	677	394	/	100	[255]
Algae-Carrageen	S, N, O	Main feedstock	852	109	/	10,000	[256]
Waste bagasse	S, N	Melamine (N) and sulphur powder (S)	110	745	200	100	[257]
Leaves	P	Phosphoric acid	601	310	90	100	[258]
Carrageenan fibers	FeS_2	$FeCl_3$ ethanol solution	265	283	75	1000	[259]
Brown seaweeds	FeS	$FeCl_3$ aqueous solution	60	385	/	2000	[260]
Carrageenan fibers	Ni_3S_4	$NiCl_2$ ethanol solution	485	297	/	1000	[261]
Coir pith	Sb_2S_3	$SbCl_3$ and cysteine	1560	443	288	100	[262]
Coir pith	Sb_2S_3	$SbCl_3$ and cysteine	1560	208	117	2000	[262]
Chlorella	MoS_2	Phosphomolybdic acid	n.a.	175	70	5000	[263]
Chlorella	MoS_2	Phosphomolybdic acid	n.a.	413	135	50	[263]
Chlorella	MoS_2, Sn	Phosphomolybdic acid, $SnSO_4$	n.a.	167	/	15,000	[264]
Popcorn	MoS_2	Aqueous solution of ammonium heptamolybdate ($(NH_4)_6Mo_7O_{24}$)	n.a.	406.9	80	200	[265]
Black fungus	Sb_2O_4	$SbCl_3$	2233	567	/	100	[266]
Blackberry seed	Sb_2O_4	$SbCl_3$	22	935	236	100	[267]
Mangosteen epicarp	$MoSe_2$	Na_2MoO_4 in ethanol, selenium in N_2H_4	289	405	108	200	[268]

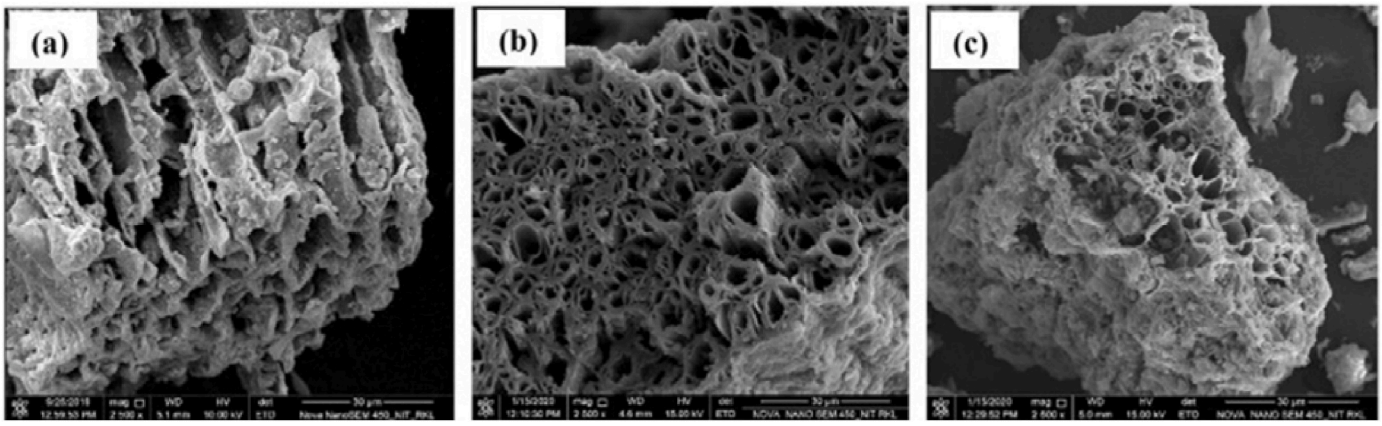

Fig. 8. Scanning electron microscope images of activated BC produced at (a) 400 °C, (b) 600 °C and (c) 900 °C, as reported in Ref. [275]. Reprinted with all permissions from Elsevier.

volume and distribution, but also on heteroatom doping of the carbonaceous matrix of BC. Heteroatom doping is an effective route for enhancing the BC activity as anode materials for NIBs. Chen et al. [251] doped a woody-derived BC by co-pyrolyzing the feedstock together with tetramethoxysilane. The tailored BC was functionalized with abundant carbonyl residue that enlarged the quasi-graphitic domains improving the Na^+ storage process. Similarly, nitrogen doping is generally achieved by using organic species that undergo to radical decomposition with the formation of highly reactive nitrogen-based radicals able to tailor the BC surface.

Romero-Cano et al. [252] used a mixture of melamine, urea and citric acid to produce a nitrogen-doped grapefruit peel-derived BC. The presence of nitrogen sites induced a more efficient sodium transport inside the pores and increased the BC disorder, leading to a stable sodium intercalation capacity of 180 mAh g^{-1} at a current density of 40 mA g^{-1}.

Alternatively, the co-pyrolysis of lignocellulosic biomass with nitrogen-rich biopolymers (such as chitosan) is a reliable route to produce nitrogen-containing BC. Enforcing this approach, Dan et al. [253] pyrolyzed a mixture of cellulose and chitosan for the production of a hybrid material composed of nitrogen-doped BC and graphene oxide, with a remarkable capacity of 227 mAh g^{-1} at 5000 mA g^{-1}. Similar results were achieved by the pyrolytic conversion of protein-rich feedstocks, such as okara [254] and honey [255]. Some authors also report the beneficial effect of sulphur [256,257] and phosphorous [258] doping, which reduces the irreversible Na^+ trapping.

Another broadly investigated strategy to tailor BC properties is the introduction of inorganic species. A clear example is represented by metal sulphide particles supported onto BC. These materials are promising as anodes for NIBs due to their high theoretical capacities, but their use is slowed down due to their poor electronic conductivity and low structural stability during the charge/discharge process. Many examples are reported in literature, based on different metal sulphides: iron [259,260], nickel [261], antimony [262] and molybdenum [263–265], deposited either as a sulphide layer or as sulphide nanoparticles onto BC surface. Similar results were achieved by depositing antimony oxides [266,267] and molybdenum and tungsten selenides [268,277].

A different approach was reported by Wang et al. [278], mixing the biomass directly with a nickel catalyst prior to the pyrolytic process to tailor the morphology of the produced particles and enhance the graphitization degree. The BC obtained using the Ni catalyst evidenced an increase of the initial CE by 40 %. Moreover, the authors evidenced the formation of thinner SEI, thus reducing the charge transfer resistance and increasing the reversible capacity.

Finally, physical activation is also a well-established route for improving the electrochemical performances of BC. Kumaresan et al. [156] reported a BC obtained from pyrolyzed flower-derived feedstock and physically activated in a controlled carbon dioxide atmosphere. The authors reported an improvement of initial capacity by 10 % after activation at 1400 °C with respect to the same BC not activated, achieving a capacity of 413 mAh g^{-1}. They correlated the enhanced activity to the introduction of defective edges on graphitic domains, with an increased disorder in their arrangement and the formation of new micropores.

3.4. The relationship between BC physicochemical and electrochemical properties: a small conundrum

The production and engineering of BC is a matter of great complexity due the simultaneous influence of multiple factors ranging from the raw materials to the pyrolytic conditions (i.e. temperature, heating rate, reactor geometry), together with possible post processing routes including activation and tailoring treatments. Depending on these processes, BC can be obtained with different structural and morphological properties, such as the specific surface area and the d-spacing among the graphitic layers, both properties affecting the electrochemical behaviour of BC. Fig. 9a allows graphically visualizing the results reported in Table 2, where all the tested BC materials displayed a d-spacing above 0.37 nm (that is higher than the graphite d-spacing of 0.34 nm and necessary for Na^+ intercalation/deintercalation [62]), but a clear trend between the values of d-spacing and the obtained electrochemical capacity cannot be defined; on the other side, the highest capacity was obtained with a BC material with a very high surface area (1930 m^2 g^{-1} [279]), although some remarkable results were reported even in cases of specific surface areas lower than 200 m^2 g^{-1}. As a guideline for further works in this field, Fig. 9b shows the dependency of the capacities reported in Table 2 with respect to the pyrolysis temperature (that represents a way to control the graphitization degree) and to the specific surface area (that is easily tuned by means of all the surface tailoring procedures described in Section 2.2). In this respect, the positive effect of increasing the pyrolysis temperature emerges, even more pronounced than the effect of the specific surface area (considering that, for instance, there are at least three reported records in which the area is higher than 500 m^2 g^{-1} but the capacity is lower than 200 mAh g^{-1}, [226,242,243]).

Data set reported in Fig. 9 provide just a general overview and not a strict regulation, since they are put together results obtained by different research groups on BC materials prepared from different raw materials and tested in different conditions in terms of electrochemical cells, electrodes formulations, combined electrolytes, and electric current densities. NIBs anode materials do not involve only pure BC, but many studies have been devoted to the preparation of doped materials with enhanced performances, as summarized in Table 3. In particular, the presence of both heteroatoms included into the carbon structure (mainly N, O, and S) and of inorganic compounds finely dispersed within the

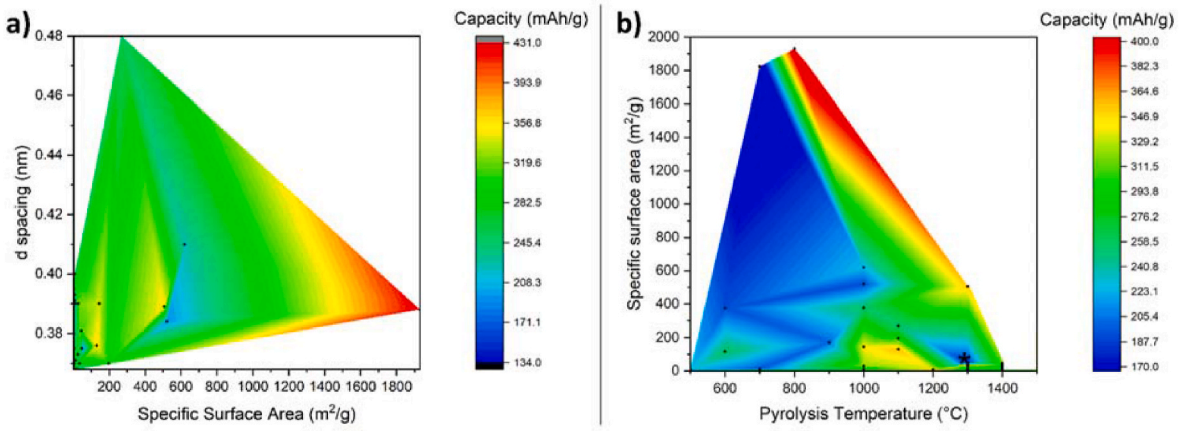

Fig. 9. a) Relationship between the highest capacity of BC in NIBs and the structural properties in terms of specific surface area and d-spacing among the graphitic layers (not all the literature references report the values of those structural parameters). b) Dependency of the capacity with respect to controlled parameters as pyrolysis temperature and specific surface area (*this datum is out of trend because the cell was tested at much higher current density as a proof of concept for fast charge/discharge applications). Data adapted from Table 2 and related references.

matrix was exploited to increase the capacity of poorly performing BC materials (even at very high current rates) [251,256,257,259,260,262–265,267].

4. Beyond NIBs: a perspective on the use of BC as electrode material in other post-Li batteries

The use of BCs as electrodes for post-lithium batteries is not limited to sodium-ion batteries. Their outstanding microstructural and electrochemical properties, which have already been discussed above, allow for the insertion of other monovalent ions (namely K^+) at low potential [280], thus making them suitable as anode materials. Moreover, their electrochemical stability towards oxidation, the electronic conductivity and the surface chemistry (*i.e.*, presence of functional groups) open up ways towards their use as positive electrodes for Metal-Sulphur and Metal-Air batteries [281].

4.1. BC as anode material for K-ion batteries

With its very low standard reduction potential (−2.936 V vs SHE) and smaller solvation shell compared to that of lithium and sodium ions in most electrolytes [282], as well as high abundance on Earth's crust (1.5 wt% of potassium compared to the total mass of the crust) [279], Potassium-ion batteries (KIBs) are nowadays considered another interesting candidate as an alternative to LIBs. Unlike Na^+, K^+ can reversibly intercalate between graphite layers with a theoretical capacity of 273 mAh g^{-1}, but generally, the huge volume change that occurs during intercalation/extraction compromises the CE and stability [283].

Due to K^+ ion elevated ionic radius, an efficient and stable KIB anode must be tailored to buffer the volume changes produced by K^+ movement inside and outside the structure. Biomass-derived carbons present a considerable variety of morphologies and microstructures, which can be tuned to fit the requirements for efficient potassium intercalation/extraction [284,285]. Those features are generally brought by a highly ordered degree of local structure but a rather disrupted order in the long-range [286]. For example, Zhang et al. [287] modelled the Von Mises stress distribution induced by K^+ insertion/extraction on different shaped-carbons: solid spheres, hollow spheres, hollow bowls and hollow multihole bowls, accompanying the obtained theoretical data with experimental investigations on different biomass-derived carbons. They showed that the more open the structure, the lower the stress produced by potassium insertion, identifying hollow multihole bowls as the best option. This result was confirmed by experimental analyses, where their best sample, BC-derived multihole bowls obtained via a hydrothermal synthesis followed by physical and then chemical activation, was able to reach capacities of 304 mAh g^{-1} after 150 cycles at a current density of 0.1 A g^{-1}, among the highest specific capacities recorded for KIB anodes.

BC composition is another critical factor that can improve the storage properties of potassium cells. Most BCs display a heteroatom-doping which is the legacy of the original biological sample's composition (intrinsic doping), but which can also be introduced during the synthetic steps (extrinsic doping) [8]. As already stated, heteroatoms positioned in place of carbon can change the local structure of the carbonaceous matrix, thus forming active sites that can electrochemically react with alkali-ions but also changing the structure of the BC itself. Recently, Lu et al. [288] proposed a pinecone-derived N-doped BC with a porous pie-like structure as anode material for KIBs. Such char was synthesized via a chemical activation reaction with molten $ZnCl_2$ and urea as nitrogen source, followed by cleaning steps. The N-doped BC was able to deliver a capacity of 267 mAh g^{-1} after 100 cycles at 50 mA g^{-1}, almost two times that obtained with the same char without N-doping. Also, the nitrogen-doped carbon was able to achieve 109 mAh g^{-1} after 1000 cycles at 5 A g^{-1}, further proving the benefits of doping. The authors also state that the activation process using $ZnCl_2$ as molten salt can work synergistically with the doping by forming a meso- and macroporous structure suitable for potassium insertion.

Several authors have also used co-doping of BCs with multiple heteroatoms to tune their properties to fit KIBs requirements. A recent example is that of Yang et al. [289], which synthesized a nitrogen, oxygen and phosphorus co-doped biomass-derived carbon as anode for KIBs. The BC, derived from sessile puffballs, was prepared by reaction of the carbon source with diethylenetriamine and tributyl phosphate in a polytetrafluoroethylene liner at 200 °C, followed by the pyrolysis in nitrogen atmosphere. The obtained NOP-BC showed a mesoporous hollow spherical structure with excellent electrochemical properties, such as a high specific capacity of 352 mAh g^{-1} after 600 cycles at 200 mA g^{-1} with a CE of about 97.5 %. Once again, the presence of voids inside the BC structure provides an ideal condition to accommodate K^+ without stressing too much the structure.

4.2. BC as cathodes for Lithium-Sulphur batteries

Another important contender for the throne held by LIBs in the global market is that of Lithium-Sulphur (Li–S) batteries. Elemental sulphur can be electrochemically lithiated at a potential of 2.1 V, with a theoretical specific capacity of 1672 mAh g^{-1}, for an overall gravimetric energy density of 2552 Wh g^{-1}, almost one order of magnitude higher than conventional LIBs [290]. Unfortunately, such a reaction brings to

the formation of the well-known polysulfides that, being soluble in most of the electrolytes used in Li–S batteries, bring to the rapid capacity decay of the battery. The polysulphide solubility and the sulphur low electric conductivity make its incorporation in conductive matrixes necessary to mitigate the polysulphide solubilization and guarantee an efficient electronic percolation through the electrode [291]. Biomass-derived carbon can be successfully employed in this field because it has strong physical and chemical adsorption properties towards polysulphides and high electric conductivity [292,293].

Pore size and surface area are among the most important parameters that define a good carbon matrix for Li–S cathodes. Generally, a high specific surface area translates into more space for sulphur to fit into [294], but it has little effect on polysulfide dissolution. The dimension of pores is, in fact, crucial: micropores (pore width <2 nm) have been proven to be suitable for polysulphides adsorption [295], while larger pores (width from 2 to 50 nm) are good for sulphur encapsulation [296]. An example is the work of Yang et al. [297], where a biomass-based carbon with both the aforementioned porosities was synthesized and tested as a cathode for Li–S batteries. Such BC was synthesized starting from garlic acid, a natural phenolic component of several plants, via a chemical activation involving a surfactant and zinc acetate. The resulting product presented both small (<5 nm) and big (>10 nm) pores and was able to operate with an initial reversible capacity of more than 800 mAh g^{-1} at 0.1C and a retention of more than 80 % after 200 cycles at 0.5C. This is due to the presence of both kinds of porosity, simultaneously able to encapsulate a good amount of sulphur (1.6 mg cm^{-2}) and to delay polysulfides dissolution.

Once again, doping the BC with heteroatoms can be beneficial for several reasons. One of them, which is shared with KIBs, is the improvement of conductivity, which is particularly important in Li–S batteries, due to the low electronic conductivity of sulphur. As already stated, this can be achieved via N-doping, which has the second advantage of creating a positively polarized defect with excellent adsorption properties towards the negative polysulfide ions [292,298]. As for KIBs applications, co-doping with BC with nitrogen, sulphur [299,300] and phosphorus [301] can be used to tune the char's properties, in this case, to encapsulate better and adsorb the polysulfides. Despite all the advantages brought by such defects, their interaction with the polysulfides remains characterized by weak van der Waals interactions [302]. In order to hinder the polysulfides diffusion and migration even further, an interesting strategy is introducing metallic compounds in the BC/sulphur cathode to have sites in which the polysulphides can chemisorb [303–305]. A recent and explicative example of this approach is that of Lin et al. [306], who synthesized a biomass-derived N, S, P co-doped carbon (soybean sprouts' stems as a precursor) and then coated such char with a layer of nitrogen-doped carbon dotted with CoSe nanoparticles. When embedded with sulphur, such compound achieved an excellent capacity of 796 mAh g^{-1} at a current as high as 4C, then reduced to 420 mAh g^{-1} after 700 cycles. Even at a low current of 0.2C, the capacity fading per cycle was about 0.04 %, which is to be considered a small value for LSBs.

4.3. BC as cathodes for metal-air batteries

The versatility of BC makes them attractive for yet another post-lithium technology: that of metal-air batteries, among which Li–O_2 is the most famous and studied. Such devices rely on the electrochemical reaction between oxygen and metal for a theoretical energy density of 3458 Wh kg^{-1} for Li–O_2 ones. In this case, a good cathode material should be able to promote the oxygen reduction reaction [307] but also its evolution, which is generally hindered by the formation of insoluble discharge products (Li_2O_2 in the case of Li–O_2 batteries), which risk blocking the pathways of O_2 and electrolytes [281,308]. Once again, heteroatom-doped BC has been proposed for this role and used in devices like Li-Air [309], Al-Air [310,311] and Zn-Air [312,313] batteries. The presence of metal compounds in carbon matrices can further improve the electrocatalytic activity of metal-air cathodes [314–316]. A recent example has been reported by Jing et al. who developed a BC co-doped with nitrogen and cobalt as cathodes for Li–O_2 batteries [317]. Such BC, synthesized from paulownia wood via pyrolysis in the presence of melamine and $CoCl_2$ as nitrogen and cobalt sources, showed 3D channels with pore sizes ranging from micro to macropores suitable for oxygen permeation. The obtained self-standing electrode was directly used as a cathode in a Li-Air battery, showing a specific capacity as high as 9 mAh cm^{-2} at 0.05 mA cm^{-2} and excellent cyclic stability at higher currents.

5. Considerations about NIBs sustainability and the role of BC

Energy storage is an unneglectable part of daily life, granting the functioning and integrity of a wide range of industrial ecosystems and infrastructures. The development of lithium-based batteries revolutionized the way to face the energy storage world [318]. Nevertheless, lithium has rapidly become a critical raw material (CRM), and its use has fed a high environmental impacting economy [4]. NIBs are among the most suitable candidate to replace lithium-based technology, but their environmental impact is more complex than could appear by a simple look. As Schneider et al. reported [319], greenhouse gas (GHS) normalized on the specific energy emitted by assembling a NIB is sensibly higher compared with a LIB, that showed more favourable life cycle assessment outputs. This consideration enlightens one of the challenges of the NIBs field: the need to increase the performances. BC could play a relevant role in the decrement of GHG emissions associated with NIBs development. As reported by Kane et al. [320], the replacement of carbon black with BC for anode production reduced the CO_2 emission by up to around 50 %. Establishing a high-value application such as NIBs production could spread BC productive sites. The lack of consolidated producers is a main drawback in the BC-based economy [321]. NIBs growth could represent the change to exploit the BC in a strategic field promoting the development of a virtuous economic model that could be established in both developed [322,323] and undeveloped countries [324,325]. Nevertheless, the real impact of BC on the GHS decrement is matter of great complexity. As reported by Matuštík et al. [326], the environmental impact of BC is strictly related to the socio-economic environment which surrounds the production platforms including both technological and logistic issues. The main problem related to the BC sustainable production is the choice between small pyrolytic units able to operate on demand and industrial scale plant that required biomass transportation on site from abroad [327]. The balance between the fuel used for biomass transportation to big plant [327] and poor efficiency of small units [328,329] is the great conundrum of the BC production and it still debate. The energetic infrastructure plays a great role on GHS produced during the BC production and a fully based renewable energetic source should be employed for significantly decreased the GHS emissions [327]. This complex scenario should be carefully considered and the best solution should be implemented considering all the aspect of BC and BC-based materials.

6. Conclusions and suggestions for future research

Electrochemical energy storage devices having enhanced energy and power densities are nowadays utterly important for the intermittent storage of renewable energy, thus reducing the dependency from fossil fuels, and fighting climate changes. Nevertheless, some critical points regarding both materials availability and technology readiness should be faced for implanting a virtuous paradigm shift of energetic market. The scarcity of critical materials represent the first relevant issue for now and the near future. As an example, the European Commission classified natural graphite as a CRM and battery-grade natural graphite as a strategic raw material; actually, graphite has also been recognized as a CRM by Japan, Canada and the US. Thanks to many appealing features, including abundance, low cost, conductivity, reversible

intercalation of sodium ion at low potential, and easiness in tailoring over its intrinsic properties, BC, the solid carbonaceous material obtained from pyrolysis of biomass waste, stands as a promising active material for developing efficient NIBs. The bio-derived, ubiquitous, renewable nature of BC, and the possibility of including its production into integrated biorefinery platforms could represent a real game changer for NIBs, one of the technologies of choice, not only to mitigate the environmental concern, but also to promote the development of sustainable energy storage applications.

Recently, there has been considerable interest about solid carbon enriched materials produced via different thermochemical techniques such as pyrolysis, however there are still obstacles to overcome towards the proper exploitation of these auspicious materials in real operational devices. Albeit they are obtained as added-value products from waste precursors (thus in principle costless), their synthesis is still not too advantageous from the economic/environmental viewpoint compared to the simple biomass waste disposal. Hence, novel and greener synthesis routes and production procedures have to be developed and optimized in view of upscaling acceleration and truly sustainable mass market deployment, paying particular attention to upgrading the processing technologies to maximize biomass-based materials utilization with high efficiency, low cost and improved added value. It is also widely assumed that more in depth analysis over the acting mechanisms of activators/dopants and knowledge over controlling and tailoring the pore geometry and interlayer carbon spacing are still necessary; indeed, unravelling the correlation between biomass precursors features/composition and resulting BC active material properties in terms of desirable nano-/micro-structural characteristics is fundamental to achieve higher energy density anode materials.

Here, we have summarized and discussed the most recent progresses towards the conversion and efficient utilization of biomass and its derived biochar as NIB negative electrode materials. The effects of various parameters involved in the synthesis methods to tailor morphology, surface area, pore structure, and composition of BC, together with the structure-activity relationships towards the development of high performing electrodes and devices have been elaborated, evidencing the possible, relevant future role of efficiently utilizing biomass and its derived biochar towards realizing sustainable energy storage devices. Many approaches are proposed in the literature to finely tune BC properties, from the choice of the proper biomass feedstock to the pre- and post-production tailoring processes. The complexity of relationship between BC features and electrochemical performances is elusive, but it emerged the key role of post-production modifications for boosting BC performance.

Similarly, NIBs are still some steps away from production and commercialization on a large-scale, and BC-based NIBs stand as one of the candidates to lead the transition to a new energy economy paradigm. Several challenges remain and the proper linkage between the BC production and biomass waste utilization plays a vital role in reducing the amount of waste being thrown and discarded by, for instance, agricultural, landfill, and sewage sectors, and converting it into more valuable products, while concurrently designing high-performance and fully bio-derived energy storage devices and helping in lowering pollution. In this respect, the present review is expected to inspire additional future research into the smart production of BC from biomass waste and its application as high added value active material in next generation batteries.

Declaration of competing interest

The authors declare no competing interests.

Data availability

No data was used for the research described in the article.

Acknowledgements

Financial support from the Italian Government, Ministry of Education, Universities and Research – MIUR (PRIN 2017 “TRUST - Towards sustainable, high-performing, all-solid-state sodium-ion batteries” funding n. 2017MCEEY4 - CUP E16C19000290006) is gratefully acknowledged.

This study was carried out within the MOST – Sustainable Mobility Center and received funding from the European Union Next-GenerationEU (PIANO NAZIONALE DI RIPRESA E RESILIENZA – PNRR e MISSIONE 4 COMPONENTE 2, INVESTIMENTO 1.4 e D.D. 1033 June 17, 2022, CN00000023). The authors thank the European Union—NextGenerationEU (National Sustainable Mobility Center CN00000023, Italian Ministry of University and Research Decree n. 1033–17/06/2022, Spoke 11—Innovative Materials & Lightweighting). This manuscript reflects only the authors’ views and opinions, neither the European Union nor the European Commission can be considered responsible for them.

A.P. gratefully acknowledges the Italian Ministry for University and Research (MUR) for funding under the D.M. 1062/2021 program.

Appendix A. Supplementary data

Supplementary data to this article can be found online at https://doi.org/10.1016/j.rser.2024.114304.

References

[1] Lebedeva N., Ruiz Ruiz V., Bielewski M., Blagoeva D., Pilenga A. Batteries technology development report 2020. No JRC123165 2020.
[2] Lu L, Han X, Li J, Hua J, Ouyang M. A review on the key issues for lithium-ion battery management in electric vehicles. J Power Sources 2013;226:272–88.
[3] Lavagna L, Meligrana G, Gerbaldi C, Tagliaferro A, Bartoli M. Graphene and lithium-based battery electrodes: a review of recent literature. Energies 2020;13:4867.
[4] Tarascon J-M. Is lithium the new gold? Nat Chem 2010;2:510.
[5] Nayak PK, Yang L, Brehm W, Adelhelm P. From lithium-ion to sodium-ion batteries: advantages, challenges, and surprises. Angew Chem Int Ed 2018;57:102–20.
[6] Abraham KM. How comparable are sodium-ion batteries to lithium-ion Counterparts? ACS Energy Lett 2020;5:3544–7.
[7] Guo Z, Qian G, Wang C, Zhang G, Yin R, Liu W-D, et al. Progress in electrode materials for the industrialization of sodium-ion batteries. Prog Nat Sci: Mater Int 2023;33:1–7.
[8] Goikolea E, Palomares V, Wang S, de Larramendi IR, Guo X, Wang G, et al. Na-ion batteries—Approaching old and new challenges. Adv Energy Mater 2020;10:2002055.
[9] Chen L, Fiore M, Wang JE, Ruffo R, Kim D-K, Longoni G. Readiness level of sodium-ion battery technology: a materials review. Advanced Sustainable Systems 2018;2:1700153.
[10] Zuo W, Innocenti A, Zarrabeitia M, Bresser D, Yang Y, Passerini S. Layered oxide cathodes for sodium-ion batteries: storage mechanism, electrochemistry, and techno-economics. Accounts Chem Res 2023;56:284–96.
[11] Yadav P, Shelke V, Patrike A, Shelke M. Sodium-based batteries: development, commercialization journey and new emerging chemistries. Oxford Open Materials Science 2022;3.
[12] Hasa I, Barker J, Elia GA, Passerini S. Sodium systems | low temperature: overview. Reference Module in chemistry, molecular Sciences and chemical engineering. Elsevier; 2023.
[13] Northvolt develops state-of-the-art sodium-ion battery validated at 160 Wh/kg. 2023. https://northvolt.com/articles/northvolt-sodium-ion/.
[14] Chayambuka K, Mulder G, Danilov DL, Notten PH. Sodium-ion battery materials and electrochemical properties reviewed. Adv Energy Mater 2018;8:1800079.
[15] Yoon G, Kim H, Park I, Kang K. Conditions for reversible Na intercalation in graphite: theoretical studies on the interplay among guest ions, solvent, and graphite host. Adv Energy Mater 2017;7:1601519.
[16] Yu P, Tang W, Wu F-F, Zhang C, Luo H-Y, Liu H, et al. Recent progress in plant-derived hard carbon anode materials for sodium-ion batteries: a review. Rare Met 2020;39:1019–33.
[17] Porporato S, Bartoli M, Piovano A, Pianta N, Tagliaferro A, Elia GA, et al. Repurposing face masks after use: from wastes to anode materials for Na-ion batteries. Batteries 2022;8:183.
[18] Liu W-J, Jiang H, Yu H-Q. Emerging applications of biochar-based materials for energy storage and conversion. Energy Environ Sci 2019;12:1751–79.
[19] Rawat S, Wang C-T, Lay C-H, Hotha S, Bhaskar T. Sustainable biochar for advanced electrochemical/energy storage applications. J Energy Storage 2023;63:107115.

[20] Alvira D, Antorán D, Manyà JJ. Plant-derived hard carbon as anode for sodium-ion batteries: a comprehensive review to guide interdisciplinary research. Chem Eng J 2022;447:137468.
[21] Bartoli M, Troiano M, Giudicianni P, Amato D, Giorcelli M, Solimene R, et al. Effect of heating rate and feedstock nature on electrical conductivity of biochar and biochar-based composites. Applications in Energy and Combustion Science 2022;12:100089.
[22] Chen W-H, Peng J, Bi XT. A state-of-the-art review of biomass torrefaction, densification and applications. Renew Sustain Energy Rev 2015;44:847–66.
[23] Peng J, Bi H, Lim C, Sokhansanj S. Study on density, hardness, and moisture uptake of torrefied wood pellets. Energy Fuels 2013;27:967–74.
[24] Bartoli M, Rosi L, Giovannelli A, Frediani P, Frediani M. Bio-oil from residues of short rotation coppice of poplar using a microwave assisted pyrolysis. J Anal Appl Pyrol 2016;119:224–32.
[25] Bartoli M, Rosi L, Giovannelli A, Frediani P, Frediani M. Characterization of bio-oil and bio-char produced by low-temperature microwave-assisted pyrolysis of olive pruning residue using various absorbers. Waste Manag Res 2020;38:213–25.
[26] Bartoli M, Rosi L, Giovannelli A, Frediani P, Frediani M. Pyrolysis of a-cellulose in a microwave multimode batch reactor. J Anal Appl Pyrol 2016;120:284–96.
[27] Garcia-Perez M, Chaala A, Pakdel H, Kretschmer D, Roy C. Characterization of bio-oils in chemical families. Biomass Bioenergy 2007;31:222–42.
[28] Huang Y, Li B, Liu D, Xie X, Zhang H, Sun H, et al. Fundamental advances in biomass autothermal/oxidative pyrolysis: a review. ACS Sustainable Chem Eng 2020;8:11888–905.
[29] Zeng K, Gauthier D, Soria J, Mazza G, Flamant G. Solar pyrolysis of carbonaceous feedstocks: a review. Sol Energy 2017;156:73–92.
[30] Huang Y-F, Chiueh P-T, Lo S-L. A review on microwave pyrolysis of lignocellulosic biomass. Sustainable Environment Research 2016;26:103–9.
[31] Garcia-Nunez J, Pelaez-Samaniego M, Garcia-Perez M, Fonts I, Abrego J, Westerhof R, et al. Historical developments of pyrolysis reactors: a review. Energy Fuels 2017;31:5751–75.
[32] Kan T, Strezov V, Evans TJ. Lignocellulosic biomass pyrolysis: a review of product properties and effects of pyrolysis parameters. Renew Sustain Energy Rev 2016;57:1126–40.
[33] Guizani C, Sanz FE, Salvador S. Influence of temperature and particle size on the single and mixed atmosphere gasification of biomass char with H_2O and CO_2. Fuel Process Technol 2015;134:175–88.
[34] Barisano D, Canneto G, Nanna F, Alvino E, Pinto G, Villone A, et al. Steam/oxygen biomass gasification at pilot scale in an internally circulating bubbling fluidized bed reactor. Fuel Process Technol 2016;141:74–81.
[35] Cheah S, Jablonski WS, Olstad JL, Carpenter DL, Barthelemy KD, Robichaud DJ, et al. Effects of thermal pretreatment and catalyst on biomass gasification efficiency and syngas composition. Green Chem 2016;18:6291–304.
[36] Tagliaferro A, Rovere M, Padovano E, Bartoli M, Giorcelli M. Introducing the novel mixed Gaussian-Lorentzian Lineshape in the analysis of the Raman signal of biochar. Nanomaterials 2020;10:1748.
[37] Oberlin A. High-resolution TEM studies of carbonization and graphitization. New York, U.S.: Marcel Dekker Inc.; 1989.
[38] Edstrom T, Lewis I. Chemical structure and graphitization: X-ray diffraction studies of graphites derived from polynuclear aromatics. Carbon 1969;7:85–91.
[39] Tomczyk A, Sokołowska Z, Boguta P. Biochar physicochemical properties: pyrolysis temperature and feedstock kind effects. Rev Environ Sci Biotechnol 2020;19:191–215.
[40] Dou X, Hasa I, Saurel D, Vaalma C, Wu L, Buchholz D, et al. Hard carbons for sodium-ion batteries: structure, analysis, sustainability, and electrochemistry. Mater Today 2019;23:87–104.
[41] Keiluweit M, Nico PS, Johnson MG, Kleber M. Dynamic molecular structure of plant biomass-derived black carbon (biochar). Environ Sci Technol 2010;44:1247–53.
[42] Franklin RE. Crystallite growth in graphitizing and non-graphitizing carbons. Proceedings of the Royal Society of London Series A Mathematical and Physical Sciences 1951;209:196–218.
[43] Shimodaira N, Masui A. Raman spectroscopic investigations of activated carbon materials. J Appl Phys 2002;92:902–9.
[44] Saito R, Hofmann M, Dresselhaus G, Jorio A, Dresselhaus MS. Raman spectroscopy of graphene and carbon nanotubes. Adv Phys 2011;60:413–550.
[45] Ferrari AC, Robertson J. Raman spectroscopy of amorphous, nanostructured, diamond like carbon, and nanodiamond. Philos Trans R Soc London, Ser A: Math Phys Eng Sci 2004;362:2477–512.
[46] Castiglioni C, Di Donato E, Tommasini M, Negri F, Zerbi G. Multi-wavelength Raman response of disordered graphitic materials: models and simulations. Synth Met 2003;139:885–8.
[47] Messina G, Santangelo S. Multi-wavelength Raman investigation of sputtered a-C film nanostructure. Surf Coating Technol 2006;200:5427–34.
[48] Couzi M, Bruneel J-L, Talaga D, Bokobza L. A multi wavelength Raman scattering study of defective graphitic carbon materials: the first order Raman spectra revisited. Carbon 2016;107:388–94.
[49] Ferrari AC, Robertson J. Interpretation of Raman spectra of disordered and amorphous carbon. Phys Rev B 2000;61:14095.
[50] Orlando A, Franceschini F, Muscas C, Pidkova S, Bartoli M, Rovere M, et al. A comprehensive review on Raman spectroscopy applications. Chemosensors 2021;9:262.
[51] Li Y, Xu S, Wu X, Yu J, Wang Y, Hu Y-S, et al. Amorphous monodispersed hard carbon micro-spherules derived from biomass as a high performance negative electrode material for sodium-ion batteries. J Mater Chem A 2015;3:71–7.
[52] Belaustegui Y, Zorita S, Fernández-Carretero F, García-Luis A, Pantò F, Stelitano S, et al. Electro-spun graphene-enriched carbon fibres with high nitrogen-contents for electrochemical water desalination. Desalination 2018;428:40–9.
[53] Irisarri E, Ponrouch A, Palacin MR. Hard carbon negative electrode materials for sodium-ion batteries. J Electrochem Soc 2015;162:A2476.
[54] Wang K, Jin Y, Sun S, Huang Y, Peng J, Luo J, et al. Low-cost and high-performance hard carbon anode materials for sodium-ion batteries. ACS Omega 2017;2:1687–95.
[55] Tuinstra F, Koenig JL. Raman spectrum of graphite. J Chem Phys 1970;53:1126–30.
[56] Lehman JH, Terrones M, Mansfield E, Hurst KE, Meunier V. Evaluating the characteristics of multiwall carbon nanotubes. Carbon 2011;49:2581–602.
[57] Messina G, Paoletti A, Santangelo S, Tagliaferro A, Tucciarone A. Nature of non-D and non-G bands in Raman spectra of a-C:H(N) films grown by reactive sputtering. J Appl Phys 2001;89:1053–8.
[58] Milone C, Shahul Hameed AR, Piperopoulos E, Santangelo S, Lanza M, Galvagno S. Catalytic wet air oxidation of p-coumaric acid over carbon nanotubes and activated carbon. Ind Eng Chem Res 2011;50:9043–53.
[59] Thomsen C, Reich S. Double resonant Raman scattering in graphite. Phys Rev Lett 2000;85:5214.
[60] Zhang T, Mao J, Liu X, Xuan M, Bi K, Zhang XL, et al. Pinecone biomass-derived hard carbon anodes for high-performance sodium-ion batteries. RSC Adv 2017;7:41504–11.
[61] Yao X, Ke Y, Ren W, Wang X, Xiong F, Yang W, et al. Defect-rich soft carbon porous nanosheets for fast and high-capacity sodium-ion storage. Adv Energy Mater 2019;9:1803260.
[62] Xiao B, Rojo T, Li X. Hard carbon as sodium-ion battery anodes: progress and challenges. ChemSusChem 2019;12:133–44.
[63] Weaving JS, Lim A, Millichamp J, Neville TP, Ledwoch D, Kendrick E, et al. Elucidating the sodiation mechanism in hard carbon by operando Raman spectroscopy. ACS Appl Energy Mater 2020;3:7474–84.
[64] Belaustegui Y, Pantò F, Urbina L, Corcuera MA, Eceiza A, Palella A, et al. Bacterial-cellulose-derived carbonaceous electrode materials for water desalination via capacitive method: the crucial role of defect sites. Desalination 2020;492:114596.
[65] Xiao L, Lu H, Fang Y, Sushko ML, Cao Y, Ai X, et al. Low-defect and low-porosity hard carbon with high coulombic efficiency and high capacity for practical sodium ion battery anode. Adv Energy Mater 2018;8:1703238.
[66] Lou Z, Wang H, Wu D, Sun F, Gao J, Lai X, et al. Microcrystalline regulation of bituminous coal derived hard carbon by pre-oxidation strategy for improved sodium-ion storage. Fuel 2022;310:122072.
[67] Ding J, Zhang Y, Huang Y, Wang X, Sun Y, Guo Y, et al. Sulfur and phosphorus co-doped hard carbon derived from oak seeds enabled reversible sodium spheres filling and plating for ultra-stable sodium storage. J Alloys Compd 2021;851:156791.
[68] Zhu C, Akiyama T. Cotton derived porous carbon via an MgO template method for high performance lithium ion battery anodes. Green Chem 2016;18:2106–14.
[69] Krishna R, Wade J, Jones AN, Lasithiotakis M, Mummery PM, Marsden BJ. An understanding of lattice strain, defects and disorder in nuclear graphite. Carbon 2017;124:314–33.
[70] Soltani N, Bahrami A, Giebeler L, Gemming T, Mikhailova D. Progress and challenges in using sustainable carbon anodes in rechargeable metal-ion batteries. Prog Energy Combust Sci 2021;87:100929.
[71] Franklin RE. Crystallite growth in graphitizing and non-graphitizing carbons. Proceedings of the Royal Society A 1951;209:196–218.
[72] Hu H-Y, Xiao Y, Ling W, Wu Y-B, Wang P, Tan S-J, et al. A stable biomass-derived hard carbon anode for high-performance sodium-ion full battery. Energy Technol 2021;9:2000730.
[73] Hou B-H, Wang Y-Y, Ning Q-L, Li W-H, Xi X-T, Yang X, et al. Self-supporting, flexible, additive-free, and scalable hard carbon paper self-interwoven by 1D microbelts: superb room/low-temperature sodium storage and working mechanism. Adv Mater 2019;31:1903125.
[74] Nair RR, Mondal MM, Weichgrebe D. Biochar from co-pyrolysis of urban organic wastes—investigation of carbon sink potential using ATR-FTIR and TGA. Biomass Conversion and Biorefinery 2022;12:4729–43.
[75] Bandosz T. J.,Surface chemistry of carbon materials. Carbon materials for Catalysis 2008:45–92.
[76] Radovic LR. Physicochemical Properties of Carbon Materials: A Brief Overview. Carbon materials for catalysis 2008:1–44.
[77] Zhang X, Zhang S, Yang H, Shao J, Chen Y, Liao X, et al. Generalized two-dimensional correlation infrared spectroscopy to reveal mechanisms of CO_2 capture in nitrogen enriched biochar. Proc Combust Inst 2017;36:3933–40.
[78] Nair RR, Mondal MM, Weichgrebe D. Biochar from co-pyrolysis of urban organic wastes—investigation of carbon sink potential using ATR-FTIR and TGA. Biomass Conversion and Biorefinery; 2020. p. 1–15.
[79] Cheng B-H, Zeng RJ, Jiang H. Recent developments of post-modification of biochar for electrochemical energy storage. Bioresour Technol 2017;246:224–33.
[80] Scott SL, Crudden CM, Jones CW. Nanostructured catalysts. Chicago, U.S.: Springer Science & Business Media; 2008.
[81] Burakov AE, Galunin EV, Burakova IV, Kucherova AE, Agarwal S, Tkachev AG, et al. Adsorption of heavy metals on conventional and nanostructured materials for wastewater treatment purposes: a review. Ecotoxicol Environ Saf 2018;148:702–12.
[82] Al-Jumaili A, Alancherry S, Bazaka K, Jacob MV. Review on the antimicrobial properties of carbon nanostructures. Materials 2017;10:1066.

[83] Bezzon VD, Montanheiro TL, de Menezes BR, Ribas RG, Righetti VA, Rodrigues KF, et al. Carbon nanostructure-based sensors: a brief review on recent advances. Adv Mater Sci Eng 2019;2019:1–21.
[84] Zhao Z-G, Ci L-J, Cheng H-M, Bai J-B. The growth of multi-walled carbon nanotubes with different morphologies on carbon fibers. Carbon 2005;43:663–5.
[85] Kong H. Hybrids of carbon nanotubes and graphene/graphene oxide. Curr Opin Solid State Mater Sci 2013;17:31–7.
[86] Zhang J, Tahmasebi A, Omoriyekomwan JE, Yu J. Production of carbon nanotubes on bio-char at low temperature via microwave-assisted CVD using Ni catalyst. Diam Relat Mater 2019;91:98–106.
[87] Zhang J, Tahmasebi A, Omoriyekomwan JE, Yu J. Microwave-assisted synthesis of biochar-carbon-nanotube-NiO composite as high-performance anode materials for lithium-ion batteries. Fuel Process Technol 2021;213:106714.
[88] Norouzi O, Maria FD, Dutta A. Biochar-based composites as electrode active materials in hybrid supercapacitors with particular focus on surface topography and morphology. J Energy Storage 2020;29:101291.
[89] Bartoli M, Giorcelli M, Rovere M, Jagdale P, Tagliaferro A, Chae M, et al. Shape tunability of carbonized cellulose nanocrystals. SN Appl Sci 2019;1:1661–76.
[90] Folarin OM, Sadiku ER, Maity A. Polymer-noble metal nanocomposites. Int. J. Phys. Sci. 2011;6:4869–82.
[91] Dobrzański L, Pawlyta M, Krztoń A, Liszka B, Labisz K. Synthesis and characterization of carbon nanotubes decorated with platinum nanoparticles. Journal of Achievements in Materials and Manufacturing Engineering 2010;39:184–9.
[92] Kuzminykh Y, Dabirian A, Reinke M, Hoffmann P. High vacuum chemical vapour deposition of oxides: a review of technique development and precursor selection. Surf Coating Technol 2013;230:13–21.
[93] Liu J, Jiang J, Meng Y, Aihemaiti A, Xu Y, Xiang H, et al. Preparation, environmental application and prospect of biochar-supported metal nanoparticles: a review. J Hazard Mater 2020;388:122026.
[94] Jing S, Ding P, Zhang Y, Liang H, Yin S, Tsiakaras P. Lithium-sulfur battery cathodes made of porous biochar support CoFe@NC metal nanoparticles derived from Prussian blue analogues. Ionics 2019;25:5297–304.
[95] Madagalam M, Bartoli M, Tagliaferro A, Carrara S. Bismuth-nanocomposites modified SPCEs for non-enzymatic electrochemical sensors. IEEE Sensor J 2021;21:11155–62.
[96] Salimi P, Norouzi O, Pourhosseini SEM. Two-step synthesis of nanohusk Fe_3O_4 embedded in 3D network pyrolytic marine biochar for a new generation of anode materials for Lithium-Ion batteries. J Alloys Compd 2019;786:930–7.
[97] Zeng J, Jagdale P, Lourenço MAO, Farkhondehfal MA, Sassone D, Bartoli M, et al. Biochar-supported BiO_x for effective Electrosynthesis of formic acid from carbon dioxide reduction. Crystals 2021;11:363.
[98] Shen Y. Carbothermal synthesis of metal-functionalized nanostructures for energy and environmental applications. J Mater Chem A 2015;3:13114–88.
[99] Tamborrino V, Costamagna G, Bartoli M, Rovere M, Jagdale P, Lavagna L, et al. Catalytic oxidative desulphurization of pyrolytic oils to fuels over different waste derived carbon-based catalysts. Fuel 2021;296:120693.
[100] Li P, Lin K, Fang Z, Wang K. Enhanced nitrate removal by novel bimetallic Fe/Ni nanoparticles supported on biochar. J Clean Prod 2017;151:21–33.
[101] Wu H, Feng Q, Yang H, Alam E, Gao B, Gu D. Modified biochar supported Ag/Fe nanoparticles used for removal of cephalexin in solution: characterization, kinetics and mechanisms. Colloids Surf A Physicochem Eng Asp 2017;517:63–71.
[102] Nisticò R, Guerretta F, Benzi P, Magnacca G. Chitosan-derived biochars obtained at low pyrolysis temperatures for potential application in electrochemical energy storage devices. Int J Biol Macromol 2020;164:1825–31.
[103] Di Noto V, Negro E, Patil B, Lorandi F, Boudjelida S, Bang YH, et al. Hierarchical metal-[carbon nitride shell/carbon core] electrocatalysts: a promising new general approach to Tackle the ORR Bottleneck in low-temperature fuel cells. ACS Catal 2022;12:12291–301.
[104] Lei H, Li J, Zhang X, Ma L, Ji Z, Wang Z, et al. A review of hard carbon anode: rational design and advanced characterization in potassium ion batteries. InfoMat 2022;4:e12272.
[105] Serp P, Figueiredo JL. Carbon materials for Catalysis. 2008.
[106] Xu X, Zheng Y, Gao B, Cao X. N-doped biochar synthesized by a facile ball-milling method for enhanced sorption of CO_2 and reactive red. Chem Eng J 2019;368:564–72.
[107] Alvira D, Antorán D, Vidal M, Sebastian V, Manyà JJ. Vine Shoots-derived hard carbons as anodes for sodium-ion batteries: role of annealing temperature in regulating their structure and morphology. Batteries & Supercaps 2023;6:e202300233.
[108] Wang X, Liu Y, Zhu L, Li Y, Wang K, Qiu K, et al. Biomass derived N-doped biochar as efficient catalyst supports for CO_2 methanation. J CO2 Util 2019;34:733–41.
[109] Suo F, You X, Ma Y, Li Y. Rapid removal of triazine pesticides by P doped biochar and the adsorption mechanism. Chemosphere 2019;235:918–25.
[110] Cheah S, Malone SC, Feik CJ. Speciation of sulfur in biochar produced from pyrolysis and gasification of oak and corn Stover. Environ Sci Technol 2014;48:8474–80.
[111] Leng L, Liu R, Xu S, Mohamed BA, Yang Z, Hu Y, et al. An overview of sulfur-functional groups in biochar from pyrolysis of biomass. J Environ Chem Eng 2022;10:107185.
[112] O'Connor D, Peng T, Li G, Wang S, Duan L, Mulder J, et al. Sulfur-modified rice husk biochar: a green method for the remediation of mercury contaminated soil. Sci Total Environ 2018;621:819–26.
[113] Sui L, Tang C, Du Q, Zhao Y, Cheng K, Yang F. Preparation and characterization of boron-doped corn straw biochar: Fe (II) removal equilibrium and kinetics. J Environ Sci 2021;106:116–23.
[114] Yao Q, Borjihan Q, Qu H, Guo Y, Zhao Z, Qiao L, et al. Cow dung-derived biochars engineered as antibacterial agents for bacterial decontamination. J Environ Sci 2021;105:33–43.
[115] Bamdad H, Hawboldt K. Comparative study between physicochemical characterization of biochar and metal organic frameworks (MOFs) as gas adsorbents. Can J Chem Eng 2016;94:2114–20.
[116] Tougaard S. Surface analysis | X-ray photoelectron spectroscopy. Encyclopedia of Analytical Science 2019:400–9.
[117] Reiche S, Blume R, Zhao XC, Su D, Kunkes E, Behrens M, et al. Reactivity of mesoporous carbon against water – an in-situ XPS study. Carbon 2014;77:175–83.
[118] Kumar U, Wu J, Sharma N, Sahajwalla V. Biomass derived high areal and specific capacity hard carbon anodes for sodium-ion batteries. Energy Fuel 2021;35:1820–30.
[119] Lee HW, Kim Y-M, Kim S, Ryu C, Park SH, Park Y-K. Review of the use of activated biochar for energy and environmental applications. Carbon letters 2018;26:1–10.
[120] Ahmadpour A, Do D. The preparation of active carbons from coal by chemical and physical activation. Carbon 1996;34:471–9.
[121] Azargohar R, Dalai A. Steam and KOH activation of biochar: experimental and modeling studies. Microporous Mesoporous Mater 2008;110:413–21.
[122] Paul R, Zemlyanov D, Roy AK, Voevodin AA. Chapter 3 - characterization techniques and analytical methods of carbon-based materials for energy applications. In: Paul R, Etacheri V, Wang Y, Lin C-T, editors. Carbon based nanomaterials for advanced thermal and electrochemical energy storage and conversion. Elsevier; 2019. p. 63–88.
[123] Shanmuga Priya M, Divya P, Rajalakshmi R. A review status on characterization and electrochemical behaviour of biomass derived carbon materials for energy storage supercapacitors. Sustainable Chemistry and Pharmacy 2020;16:100243.
[124] Paul R, Du F, Dai L, Ding Y, Wang ZL, Wei F, et al. 3D heteroatom-doped carbon nanomaterials as multifunctional metal-free catalysts for integrated energy devices. Adv Mater 2019;31:1805598.
[125] Bouchelta C, Medjram MS, Bertrand O, Bellat J-P. Preparation and characterization of activated carbon from date stones by physical activation with steam. J Anal Appl Pyrol 2008;82:70–7.
[126] Molina-Sabio M, Gonzalez M, Rodriguez-Reinoso F, Sepúlveda-Escribano A. Effect of steam and carbon dioxide activation in the micropore size distribution of activated carbon. Carbon 1996;34:505–9.
[127] Zhang T, Walawender WP, Fan L, Fan M, Daugaard D, Brown R. Preparation of activated carbon from forest and agricultural residues through CO_2 activation. Chem Eng J 2004;105:53–9.
[128] Klei HE, Sahagian J, Sundstrom DW. Kinetics of the activated carbon-steam reaction. Ind Eng Chem Process Des Dev 1975;14:470–3.
[129] Jung S-H, Kim J-S. Production of biochars by intermediate pyrolysis and activated carbons from oak by three activation methods using CO_2. J Anal Appl Pyrol 2014;107:116–22.
[130] Franciski MA, Peres EC, Godinho M, Perondi D, Foletto EL, Collazzo GC, et al. Development of CO_2 activated biochar from solid wastes of a beer industry and its application for methylene blue adsorption. Waste Manag 2018;78:630–8.
[131] Sun C, Chen T, Huang Q, Zhan M, Li X, Yan J. Activation of persulfate by CO_2-activated biochar for improved phenolic pollutant degradation: performance and mechanism. Chem Eng J 2020;380:122519.
[132] Rajapaksha AU, Vithanage M, Ahmad M, Seo D-C, Cho J-S, Lee S-E, et al. Enhanced sulfamethazine removal by steam-activated invasive plant-derived biochar. J Hazard Mater 2015;290:43–50.
[133] Heidarinejad Z, Dehghani MH, Heidari M, Javedan G, Ali I, Sillanpää M. Methods for preparation and activation of activated carbon: a review. Environ Chem Lett 2020;18:393–415.
[134] Acemioğlu B. Removal of a reactive dye using NaOH-activated biochar prepared from peanut shell by pyrolysis process. International Journal of Coal Preparation and Utilization 2019:1–23.
[135] Han X, Chu L, Liu S, Chen T, Ding C, Yan J, et al. Removal of methylene blue from aqueous solution using porous biochar obtained by KOH activation of peanut shell biochar. Bioresources 2015;10:2836–49.
[136] Uçar S, Erdem M, Tay T, Karagöz S. Removal of lead (II) and nickel (II) ions from aqueous solution using activated carbon prepared from rapeseed oil cake by Na_2CO_3 activation. Clean Technol Environ Policy 2015;17:747–56.
[137] Wang L, Sun F, Hao F, Qu Z, Gao J, Liu M, et al. A green trace K_2CO_3 induced catalytic activation strategy for developing coal-converted activated carbon as advanced candidate for CO2 adsorption and supercapacitors. Chem Eng J 2020;383:123205.
[138] Antorán D, Alvira D, Peker ME, Malón H, Irusta S, Sebastián V, et al. Waste hemp hurd as a sustainable precursor for affordable and high-rate hard carbon-based anodes in sodium-ion batteries. Energy Fuels 2023;37:9650–61.
[139] Moreno-Castilla C, Ferro-Garcia M, Joly J, Bautista-Toledo I, Carrasco-Marin F, Rivera-Utrilla J. Activated carbon surface modifications by nitric acid, hydrogen peroxide, and ammonium peroxydisulfate treatments. Langmuir 1995;11:4386–92.
[140] Oginni O, Singh K, Oporto G, Dawson-Andoh B, McDonald L, Sabolsky E. Effect of one-step and two-step H_3PO_4 activation on activated carbon characteristics. Bioresour Technol Rep 2019;8:100307.
[141] Iriarte-Velasco U, Sierra I, Zudaire L, Ayastuy JL. Preparation of a porous biochar from the acid activation of pork bones. Food Bioprod Process 2016;98:341–53.

[142] Li H, Xiong J, Zhang G, Liang A, Long J, Xiao T, et al. Enhanced thallium (I) removal from wastewater using hypochlorite oxidation coupled with magnetite-based biochar adsorption. Sci Total Environ 2020;698:134166.
[143] Huang B-C, Jiang J, Huang G-X, Yu H-Q. Sludge biochar-based catalysts for improved pollutant degradation by activating peroxymonosulfate. J Mater Chem A 2018;6:8978–85.
[144] Grilla E, Vakros J, Konstantinou I, Manariotis ID, Mantzavinos D. Activation of persulfate by biochar from spent malt rootlets for the degradation of trimethoprim in the presence of inorganic ions. J Chem Technol Biotechnol 2020; 95:2348–58.
[145] Huang D, Wang Y, Zhang C, Zeng G, Lai C, Wan J, et al. Influence of morphological and chemical features of biochar on hydrogen peroxide activation: implications on sulfamethazine degradation. RSC Adv 2016;6:73186–96.
[146] Asher R. A lamellar compound of sodium and graphite. J Inorg Nucl Chem 1959; 10:238–49.
[147] Lenchuk O, Adelhelm P, Mollenhauer D. New insights into the origin of unstable sodium graphite intercalation compounds. Phys Chem Chem Phys 2019;21: 19378–90.
[148] Stevens D, Dahn J. The mechanisms of lithium and sodium insertion in carbon materials. J Electrochem Soc 2001;148:A803.
[149] Alvin S, Cahyadi HS, Hwang J, Chang W, Kwak SK, Kim J. Revealing the intercalation mechanisms of lithium, sodium, and potassium in hard carbon. Adv Energy Mater 2020;10:2000283.
[150] Alvin S, Yoon D, Chandra C, Cahyadi HS, Park J-H, Chang W, et al. Revealing sodium ion storage mechanism in hard carbon. Carbon 2019;145:67–81.
[151] Gomez-Martin A, Martinez-Fernandez J, Ruttert M, Winter M, Placke T, Ramirez-Rico J. Correlation of structure and performance of hard carbons as anodes for sodium ion batteries. Chem Mater 2019;31:7288–99.
[152] Bommier C, Surta TW, Dolgos M, Ji X. New mechanistic insights on Na-ion storage in nongraphitizable carbon. Nano Lett 2015;15:5888–92.
[153] Euchner H, Vinayan BP, Reddy MA, Fichtner M, Groß A. Alkali metal insertion into hard carbon–the full picture. J Mater Chem A 2020;8:14205–13.
[154] Cheng X, Li H, Zhao Z, Wang Y, Wang X. The use of in-situ Raman spectroscopy in investigating carbon materials as anodes of alkali metal-ion batteries. New Carbon Mater 2021;36:93–105.
[155] Sun N, Qiu J, Xu B. Understanding of sodium storage mechanism in hard carbons: Ongoing development under debate. Adv Energy Mater 2022:2200715.
[156] Kumaresan TK, Masilamani SA, Raman K, Karazhanov SZ, Subashchandrabose R. High performance sodium-ion battery anode using biomass derived hard carbon with engineered defective sites. Electrochim Acta 2021;368:137574.
[157] Wang K, Xu Y, Li Y, Dravid V, Wu J, Huang Y. Sodium storage in hard carbon with curved graphene platelets as the basic structural units. J Mater Chem A 2019;7: 3327–35.
[158] Ouvrard G, Jobic S. X-ray absorption spectroscopy (XAS). Springer Handbook of Inorganic Photochemistry. 2022. p. 273–302.
[159] Wang S, Yan N. X-Ray absorption spectroscopy: an indispensable tool to study single-atom catalysts. Synchrotron Radiat News 2020;33:18–26.
[160] Koningsberger DC, Prins R. X-ray absorption: principles, applications, techniques of EXAFS, SEXAFS and XANES. Wiley Interscience; 1988.
[161] Greco G, Mazzio KA, Dou X, Gericke E, Wendt R, Krumrey M, et al. Structural study of carbon-coated TiO_2 Anatase nanoparticles as high-performance anode materials for Na-ion batteries. ACS Appl Energy Mater 2019;2:7142–51.
[162] Chen J, Mohrhusen L, Ali G, Li S, Chung KY, Al-Shamery K, et al. Electrochemical mechanism investigation of Cu_2MoS_4 hollow nanospheres for fast and stable sodium ion storage. Adv Funct Mater 2019;29:1807753.
[163] Xiao W, Sun Q, Banis MN, Wang B, Liang J, Lushington A, et al. Unveiling the Interfacial instability of the phosphorus/carbon anode for sodium-ion batteries. ACS Appl Mater Interfaces 2019;11:30763–73.
[164] Jin H, Zhang T, Chuang C, Lu Y-R, Chan T-S, Du Z, et al. Synergy of black phosphorus–graphite–Polyaniline-based ternary composites for stable high reversible capacity Na-ion battery anodes. ACS Appl Mater Interfaces 2019;11: 16656–61.
[165] Deng D, Chen X, Yu L, Wu X, Liu Q, Liu Y, et al. A single iron site confined in a graphene matrix for the catalytic oxidation of benzene at room temperature. Sci Adv 2015;1:e1500462.
[166] Ellis LD, Hatchard TD, Obrovac MN. Reversible insertion of sodium in Tin. J Electrochem Soc 2012;159:A1801.
[167] Darwiche A, Marino C, Sougrati MT, Fraisse B, Stievano L, Monconduit L. Better cycling performances of bulk Sb in Na-ion batteries compared to Li-ion systems: an Unexpected electrochemical mechanism. J Am Chem Soc 2012;134:20805–11.
[168] Negro E, Nale A, Vezzù K, Pagot G, Polizzi S, Bertoncello R, et al. Hierarchical oxygen reduction reaction electrocatalysts based on $FeSn_{0.5}$ species embedded in carbon nitride-graphene based supports. Electrochim Acta 2018;280:149–62.
[169] Negro E, Bach Delpeuch A, Vezzù K, Nawn G, Bertasi F, Ansaldo A, et al. Toward Pt-free anion-exchange membrane fuel cells: Fe-Sn carbon nitride-graphene core-shell electrocatalysts for the oxygen reduction reaction. Chem Mater 2018;30: 2651–9.
[170] Baggetto L, Hah HY, Jumas JC, Johnson CE, Johnson JA, Keum JK, et al. The reaction mechanism of SnSb and Sb thin film anodes for Na-ion batteries studied by X-ray diffraction, ^{119}Sn and ^{121}Sb Mössbauer spectroscopies. J Power Sources 2014;267:329–36.
[171] Sougrati MT, Darwiche A, Liu X, Mahmoud A, Hermann RP, Jouen S, et al. Transition-metal Carbodiimides as molecular negative electrode materials for lithium- and sodium-ion batteries with excellent cycling properties. Angew Chem Int Ed 2016;55:5090–5.
[172] Liao S, Wang X, Hu H, Chen D, Zhang M, Luo J. Carbon-encapsulated Sb_6O_{13} nanoparticles for an efficient and durable sodium-ion battery anode. J Alloys Compd 2021;852:156939.
[173] Gütlich P, Schröder C, Schünemann V. Mössbauer spectroscopy - an indispensable tool in solid state research. Spectrosc Eur 2012;24:21–32.
[174] Liu M, Wang Y, Wu F, Bai Y, Li Y, Gong Y, et al. Advances in carbon materials for sodium and potassium storage. Adv Funct Mater 2022;32:2203117.
[175] Alcántara R, Ortiz GF, Lavela P, Tirado JL, Stoyanova R, Zhecheva E. EPR, NMR, and electrochemical studies of surface-modified carbon microbeads. Chem Mater 2006;18:2293–301.
[176] Yu Z-E, Lyu Y, Wang Y, Xu S, Cheng H, Mu X, et al. Hard carbon micro-nano tubes derived from kapok fiber as anode materials for sodium-ion batteries and the sodium-ion storage mechanism. Chem Commun 2020;56:778–81.
[177] Kawamura K. Electron spin resonance behavior of pitch-based carbons in the heat treatment temperature range of 1100–2000 °C. Carbon 1998;36:1227–30.
[178] Shkrob IA, Zhu Y, Marin TW, Abraham D. Reduction of carbonate electrolytes and the formation of solid-electrolyte interface (SEI) in lithium-ion batteries. 1. Spectroscopic observations of radical Intermediates generated in one-electron reduction of carbonates. J Phys Chem C 2013;117:19255–69.
[179] Zhecheva E, Stoyanova R, Jiménez-Mateos JM, Alcántara R, Lavela P, Tirado JL. EPR study on petroleum cokes annealed at different temperatures and used in lithium and sodium batteries. Carbon 2002;40:2301–6.
[180] Tampieri F, Silvestrini S, Riccò R, Maggini M, Barbon A. A comparative electron paramagnetic resonance study of expanded graphites and graphene. J Mater Chem C 2014;2:8105–12.
[181] Kubota K, Shimadzu S, Yabuuchi N, Tominaka S, Shiraishi S, Abreu-Sepulveda M, et al. Structural analysis of sucrose-derived hard carbon and correlation with the electrochemical properties for lithium, sodium, and potassium insertion. Chem Mater 2020;32:2961–77.
[182] Tomita S, Sakurai T, Ohta H, Fujii M, Hayashi S. Structure and electronic properties of carbon onions. J Chem Phys 2001;114:7477–82.
[183] Emmerich FG, Rettori C, Luengo CA. ESR in heat treated carbons from the endocarp of babassu coconut. Carbon 1991;29:305–11.
[184] Li X, Zeng X, Ren T, Zhao J, Zhu Z, Sun S, et al. The transport properties of sodium-ion in the low potential platform region of oatmeal-derived hard carbon for sodium-ion batteries. J Alloys Compd 2019;787:229–38.
[185] Xiao L, Cao Y, Henderson WA, Sushko ML, Shao Y, Xiao J, et al. Hard carbon nanoparticles as high-capacity, high-stability anodic materials for Na-ion batteries. Nano Energy 2016;19:279–88.
[186] Seidl L, Bucher N, Chu E, Hartung S, Martens S, Schneider O, et al. Intercalation of solvated Na-ions into graphite. Energy Environ Sci 2017;10:1631–42.
[187] Yu P, Tang W, Wu FF, Zhang C, Luo HY, Liu H, et al. Recent progress in plant-derived hard carbon anode materials for sodium-ion batteries: a review. Rare Met 2020;39:1019–33.
[188] Li K, Zhang J, Lin D, Wang D-W, Li B, Lv W, et al. Evolution of the electrochemical interface in sodium ion batteries with ether electrolytes. Nat Commun 2019;10: 725.
[189] Vezzù K, García-González E, Pagot G, Urones-Garrote E, Sotomayor ME, Varez A, et al. Effect of relaxations on the conductivity of $La_{1/2+1/2x}Li_{1/2-1/2x}Ti_{1-x}Al_xO_3$ fast ion conductors. Chem Mater 2022;34:5484–99.
[190] Pagot G, Vezzù K, Martinez-Cisneros CS, Antonelli C, Levenfeld B, Varez A, et al. Interplay between conductivity, matrix relaxations and composition of Ca-Polyoxyethylene polymer electrolytes. Chemelectrochem 2021;8:2459–66.
[191] Pagot G, Bertasi F, Vezzù K, Sepehr F, Luo X, Nawn G, et al. Three-dimensional catenated 1-ethyl-3-methylimidazolium halotitanate ionic liquid electrolytes for electrochemical applications. Electrochim Acta 2017;246:914–23.
[192] Di Noto V, Giffin GA, Vezzù K, Piga M, Lavina S. Broadband dielectric spectroscopy: a powerful tool for the determination of charge transfer mechanisms in ion conductors. In: Knauth P, Vona MLD, editors. Solid state proton conductors: properties and applications in fuel cells. Weinheim, Germany: John Wiley & Sons; 2012. p. 109–83.
[193] Pagot G, Garaga M, Jadhav AL, O'Donnell LF, Vezzù K, Itin B, et al. Interplay between coordination, dynamics, and conductivity mechanism in Mg/Al-catenated ionic liquid electrolytes. J Power Sources 2022;524:231084.
[194] Di Noto V, Piga M, Giffin GA, Vezzu K, Zawodzinski TA. Interplay between mechanical, electrical, and thermal relaxations in nanocomposite proton conducting membranes based on nafion and a $[(ZrO_2)(Ta_2O_5)_{0.119}]$ core-shell nanofiller. J Am Chem Soc 2012;134:19099–107.
[195] Kusoglu A, Vezzù K, Hegde GA, Nawn G, Motz AR, Sarode HN, et al. Transport and morphology of a proton Exchange membrane based on a doubly functionalized Perfluorosulfonic Imide side chain Perflourinated polymer. Chem Mater 2020;32:38–59.
[196] Kumar D, Gohel K, Kanchan DK, Mishra K. Dielectrics and battery studies on flexible nanocomposite gel polymer electrolyte membranes for sodium batteries. J Mater Sci Mater Electron 2020;31:13249–60.
[197] Salame P, Kotalgi K, Devakar M, More P. Electronic transport properties of NASICON structured $NaFe_2(PO_4)(SO_4)_2$: a potential cathode material for Na-ion batteries, synthesized using ultrasound-assisted, indirect microwave heating technique. Mater Lett 2022:313.
[198] Pagot G, Bertasi F, Nawn G, Negro E, Bach Delpeuch A, Vezzù K, et al. Effect of graphite and Copper oxide on the performance of high potential $Li[Fe_{1/3}Ni_{1/3}Co_{1/3}]PO_4$ olivine cathodes for lithium batteries. Electrochim Acta 2017;225:533–42.
[199] Pagot G, Di Noto V, Vezzù K, Barbiellini B, Toso V, Caruso A, et al. Quantum view of Li-ion high mobility at carbon coated cathode interfaces. iScience 2022: 105794.

[200] Jain A, Shin Y, Persson KA. Computational predictions of energy materials using density functional theory. Nat Rev Mater 2016;1:1–13.
[201] Urban A, Seo D-H, Ceder G. Computational understanding of Li-ion batteries. npj Comput Mater 2016;2:1–13.
[202] Alptekin H, Au H, Jensen AC, Olsson E, Goktas M, Headen TF, et al. Sodium storage mechanism investigations through structural changes in hard carbons. ACS Appl Energy Mater 2020;3:9918–27.
[203] Anji Reddy M, Helen M, Groß A, Fichtner M, Euchner H. Insight into sodium insertion and the storage mechanism in hard carbon. ACS Energy Lett 2018;3:2851–7.
[204] Senftle TP, Meyer RJ, Janik MJ, Van Duin AC. Development of a ReaxFF potential for Pd/O and application to palladium oxide formation. J Chem Phys 2013;139:044109.
[205] Huang J-X, Csányi G, Zhao J-B, Cheng J, Deringer VL. First-principles study of alkali-metal intercalation in disordered carbon anode materials. J Mater Chem A 2019;7:19070–80.
[206] Li Q, Zhang J, Zhong L, Geng F, Tao Y, Geng C, et al. Unraveling the key atomic interactions in determining the Varying Li/Na/K storage mechanism of hard carbon anodes. Adv Energy Mater 2022;12:2201734.
[207] Au H, Alptekin H, Jensen AC, Olsson E, O'Keefe CA, Smith T, et al. A revised mechanistic model for sodium insertion in hard carbons. Energy Environ Sci 2020;13:3469–79.
[208] Li J, Peng C, Li J, Wang J, Zhang H. Insight into sodium storage Behaviors in hard carbon by ReaxFF molecular dynamics simulation. Energy & Fuels; 2022.
[209] Li J, Peng C, Wang J, Li J, Zhang H. Towards an atomistic understanding of hard carbon electrode materials and sodium behaviors. Diam Relat Mater 2022;129:109355.
[210] Kizzire DG, Richter AM, Harper DP, Keffer DJ. Lithium and sodium ion binding mechanisms and diffusion rates in lignin-based hard carbon models. ACS Omega 2021;6:19883–92.
[211] Tenhaeff WE, Rios O, More K, McGuire MA. Highly robust lithium ion battery anodes from lignin: an abundant, renewable, and low-cost material. Adv Funct Mater 2014;24:86–94.
[212] Doeff MM, Ma Y, Visco SJ, De Jonghe LC. Electrochemical insertion of sodium into carbon. J Electrochem Soc 1993;140:L169.
[213] Yamamoto H, Muratsubaki S, Kubota K, Fukunishi M, Watanabe H, Kim J, et al. Synthesizing higher-capacity hard-carbons from cellulose for Na- and K-ion batteries. J Mater Chem A 2018;6:16844–8.
[214] Simone V, Boulineau A, de Geyer A, Rouchon D, Simonin L, Martinet S. Hard carbon derived from cellulose as anode for sodium ion batteries: Dependence of electrochemical properties on structure. J Energy Chem 2016;25:761–8.
[215] Lotfabad EM, Ding J, Cui K, Kohandehghan A, Kalisvaart WP, Hazelton M, et al. High-density sodium and lithium ion battery anodes from banana peels. ACS Nano 2014;8:7115–29.
[216] Nita C, Zhang B, Dentzer J, Matei Ghimbeu C. Hard carbon derived from coconut shells, walnut shells, and corn silk biomass waste exhibiting high capacity for Na-ion batteries. J Energy Chem 2021;58:207–18.
[217] Ding J, Wang H, Li Z, Kohandehghan A, Cui K, Xu Z, et al. Carbon Nanosheet frameworks derived from peat moss as high performance sodium ion battery anodes. ACS Nano 2013;7:11004–15.
[218] Wang H, Yu W, Shi J, Mao N, Chen S, Liu W. Biomass derived hierarchical porous carbons as high-performance anodes for sodium-ion batteries. Electrochim Acta 2016;188:103–10.
[219] Shen F, Luo W, Dai J, Yao Y, Zhu M, Hitz E, et al. Ultra-thick, low-tortuosity, and mesoporous wood carbon anode for high-performance sodium-ion batteries. Adv Energy Mater 2016;6:1600377.
[220] Raj KA, Panda MR, Dutta DP, Mitra S. Bio-derived mesoporous disordered carbon: an excellent anode in sodium-ion battery and full-cell lab prototype. Carbon 2019;143:402–12.
[221] Fu H, Xu Z, Li R, Guan W, Yao K, Huang J, et al. Network carbon with macropores from apple pomace for stable and high areal capacity of sodium storage. ACS Sustainable Chem Eng 2018;6:14751–8.
[222] Zhang Y, Li X, Dong P, Wu G, Xiao J, Zeng X, et al. Honeycomb-like hard carbon derived from pine pollen as high-performance anode material for sodium-ion batteries. ACS Appl Mater Interfaces 2018;10:42796–803.
[223] Wang P, Zhu K, Ye K, Gong Z, Liu R, Cheng K, et al. Three-dimensional biomass derived hard carbon with reconstructed surface as a free-standing anode for sodium-ion batteries. J Colloid Interface Sci 2020;561:203–10.
[224] Wang C, Huang J, Qi H, Cao L, Xu Z, Cheng Y, et al. Controlling pseudographtic domain dimension of dandelion derived biomass carbon for excellent sodium-ion storage. J Power Sources 2017;358:85–92.
[225] Izanzar I, Dahbi M, Kiso M, Doubaji S, Komaba S, Saadoune I. Hard carbons issued from date palm as efficient anode materials for sodium-ion batteries. Carbon 2018;137:165–73.
[226] Zhang F, Yao Y, Wan J, Henderson D, Zhang X, Hu L. High temperature carbonized grass as a high performance sodium ion battery anode. ACS Appl Mater Interfaces 2017;9:391–7.
[227] Rios CdMS, Simone V, Simonin L, Martinet S, Dupont C. Biochars from various biomass types as precursors for hard carbon anodes in sodium-ion batteries. Biomass Bioenergy 2018;117:32–7.
[228] Luo W, Schardt J, Bommier C, Wang B, Razink J, Simonsen J, et al. Carbon nanofibers derived from cellulose nanofibers as a long-life anode material for rechargeable sodium-ion batteries. J Mater Chem A 2013;1:10662–6.
[229] Zhang X, Hu J, Chen X, Zhang M, Huang Q, Du X, et al. Microtubular carbon fibers derived from bamboo and wood as sustainable anodes for lithium and sodium ion batteries. J Porous Mater 2019;26:1821–30.
[230] Zhu H, Shen F, Luo W, Zhu S, Zhao M, Natarajan B, et al. Low temperature carbonization of cellulose nanocrystals for high performance carbon anode of sodium-ion batteries. Nano Energy 2017;33:37–44.
[231] Jin J, Yu B-j, Shi Z-q, Wang C-y, Chong C-b. Lignin-based electrospun carbon nanofibrous webs as free-standing and binder-free electrodes for sodium ion batteries. J Power Sources 2014;272:800–7.
[232] Cong L, Tian G, Luo D, Ren X, Xiang X. Hydrothermally assisted transformation of corn stalk wastes into high-performance hard carbon anode for sodium-ion batteries. J Electroanal Chem 2020;871:114249.
[233] Yang T, Niu X, Qian T, Shen X, Zhou J, Xu N, et al. Half and full sodium-ion batteries based on maize with high-loading density and long-cycle life. Nanoscale 2016;8:15497–504.
[234] Wang J, Yan L, Ren Q, Fan L, Zhang F, Shi Z. Facile hydrothermal treatment route of reed straw-derived hard carbon for high performance sodium ion battery. Electrochim Acta 2018;291:188–96.
[235] Wang Q, Zhu X, Liu Y, Fang Y, Zhou X, Bao J. Rice husk-derived hard carbons as high-performance anode materials for sodium-ion batteries. Carbon 2018;127:658–66.
[236] Yu C, Hou H, Liu X, Yao Y, Liao Q, Dai Z, et al. Old-loofah-derived hard carbon for long cyclicity anode in sodium ion battery. Int J Hydrogen Energy 2018;43:3253–60.
[237] Lyu T, Lan X, Liang L, Lin X, Hao C, Pan Z, et al. Natural mushroom spores derived hard carbon plates for robust and low-potential sodium ion storage. Electrochim Acta 2021;365:137356.
[238] Dahbi M, Kiso M, Kubota K, Horiba T, Chafik T, Hida K, et al. Synthesis of hard carbon from argan shells for Na-ion batteries. J Mater Chem A 2017;5:9917–28.
[239] Lv W, Wen F, Xiang J, Zhao J, Li L, Wang L, et al. Peanut shell derived hard carbon as ultralong cycling anodes for lithium and sodium batteries. Electrochim Acta 2015;176:533–41.
[240] Cao L, Hui W, Xu Z, Huang J, Zheng P, Li J, et al. Rape seed shuck derived-lamellar hard carbon as anodes for sodium-ion batteries. J Alloys Compd 2017;695:632–7.
[241] Zhang N, Liu Q, Chen W, Wan M, Li X, Wang L, et al. High capacity hard carbon derived from lotus stem as anode for sodium ion batteries. J Power Sources 2018;378:331–7.
[242] Tian Z, Sun S, Zhao X, Yang M, Xu C. Phoenix tree leaves-derived biomass carbons for sodium-ion batteries. Functional Materials Letters 2018;11:1840008.
[243] Arie AA, Tekin B, Demir E, Demir-Cakan R. Hard carbons derived from waste tea bag powder as anodes for sodium ion battery. Mater Technol 2019;34:515–24.
[244] Meng X, Savage PE, Deng D. Trash to Treasure: from harmful algal blooms to high-performance electrodes for sodium-ion batteries. Environ Sci Technol 2015;49:12543–50.
[245] Darjazi H, Staffolani A, Sbrascini L, Bottoni L, Tossici R, Nobili F. Sustainable anodes for lithium- and sodium-ion batteries based on coffee ground-derived hard carbon and green binders. Energies 2020;13:6216.
[246] Sajjadi B, Zubatiuk T, Leszczynska D, Leszczynski J, Chen WY. Chemical activation of biochar for energy and environmental applications: a comprehensive review. Rev Chem Eng 2019;35:777–815.
[247] Torsello D, Ghigo G, Giorcelli M, Bartoli M, Rovere M, Tagliaferro A. Tuning the microwave electromagnetic properties of biochar-based composites by annealing. Carbon Trends 2021:100062.
[248] Morita R, Gotoh K, Kubota K, Komaba S, Hashi K, Shimizu T, et al. Correlation of carbonization condition with metallic property of sodium clusters formed in hard carbon studied using 23Na nuclear magnetic resonance. Carbon 2019;145:712–5.
[249] Saavedra Rios CdM, Simone V, Simonin L, Martinet S, Dupont C. Biochars from various biomass types as precursors for hard carbon anodes in sodium-ion batteries. Biomass Bioenergy 2018;117:32–7.
[250] Johnson JM, Coleman MD, Gesch R, Jaradat A, Mitchell R, Reicosky D, et al. Biomass-bioenergy crops in the United States: a changing paradigm. The Americas Journal of Plant Science and Biotechnology 2007;1:1–28.
[251] Chen L, Bai L, Yeo J, Wei T, Chen W, Fan Z. Wood-derived carbon with selectively introduced C═O groups toward stable and high capacity anodes for sodium storage. ACS Appl Mater Interfaces 2020;12:27499–507.
[252] Romero-Cano LA, García-Rosero H, Carrasco-Marín F, Pérez-Cadenas AF, González-Gutiérrez LV, Zárate-Guzmán AI, et al. Surface functionalization to abate the irreversible capacity of hard carbons derived from grapefruit peels for sodium-ion batteries. Electrochim Acta 2019;326:134973.
[253] Dan R, Chen W, Xiao Z, Li P, Liu M, Chen Z, et al. N-doped biomass carbon/reduced graphene oxide as a high-performance anode for sodium-ion batteries. Energy Fuels 2020;34:3923–30.
[254] Yang T, Qian T, Wang M, Shen X, Xu N, Sun Z, et al. A sustainable route from biomass byproduct okara to high content nitrogen-doped carbon sheets for efficient sodium ion batteries. Adv Mater 2016;28:539–45.
[255] Zhang Y, Chen L, Meng Y, Xie J, Guo Y, Xiao D. Lithium and sodium storage in highly ordered mesoporous nitrogen-doped carbons derived from honey. J Power Sources 2016;335:20–30.
[256] Lu M, Yu W, Shi J, Liu W, Chen S, Wang X, et al. Self-doped carbon architectures with heteroatoms containing nitrogen, oxygen and sulfur as high-performance anodes for lithium- and sodium-ion batteries. Electrochim Acta 2017;251:396–406.
[257] Wan H, Hu X. Nitrogen/sulfur co-doped disordered porous biocarbon as high performance anode materials of lithium/sodium ion batteries. Int J Hydrogen Energy 2019;44:22250–62.
[258] Zhu Y, Huang Y, Chen C, Wang M, Liu P. Phosphorus-doped porous biomass carbon with ultra-stable performance in sodium storage and lithium storage. Electrochim Acta 2019;321:134698.

[259] Li D, Sun Y, Chen S, Yao J, Zhang Y, Xia Y, et al. Highly porous FeS/carbon fibers derived from Fe-carrageenan biomass: high-capacity and durable anodes for sodium-ion batteries. ACS Appl Mater Interfaces 2018;10:17175–82.
[260] Liu H, Lv C, Chen S, Song X, Liu B, Sun J, et al. Fe-alginate biomass-derived FeS/3D interconnected carbon nanofiber aerogels as anodes for high performance sodium-ion batteries. J Alloys Compd 2019;795:54–9.
[261] Guo R, Li D, Lv C, Wang Y, Zhang H, Xia Y, et al. Porous Ni3S4/C aerogels derived from carrageenan-Ni hydrogels for high-performance sodium-ion batteries anode. Electrochim Acta 2019;299:72–9.
[262] Mullaivananathan V, Kalaiselvi N. Sb2S3 added bio-carbon: Demonstration of potential anode in lithium and sodium-ion batteries. Carbon 2019;144:772–80.
[263] Luo F, Xia X, Zeng L, Chen X, Feng X, Wang J, et al. A composite of ultra-fine few-layer MoS_2 structures embedded on N,P-co-doped bio-carbon for high-performance sodium-ion batteries. New J Chem 2020;44:2046–52.
[264] Zeng L, Luo F, Xia X, Yang M-Q, Xu L, Wang J, et al. An Sn doped 1T–2H MoS2 few-layer structure embedded in N/P co-doped bio-carbon for high performance sodium-ion batteries. Chem Commun 2019;55:3614–7.
[265] Lin M, Deng M, Zhou C, Shu Y, Yang L, Ouyang L, et al. Popcorn derived carbon enhances the cyclic stability of MoS_2 as an anode material for sodium-ion batteries. Electrochim Acta 2019;309:25–33.
[266] Zhang X, Li P, Zang R, Wang S, Zhu Y, Li C, et al. Antimony/porous biomass carbon nanocomposites as high-capacity anode materials for sodium-ion batteries. Chem Asian J 2017;12:116–21.
[267] Dutta DP. Composites of Sb2O4 and biomass-derived mesoporous disordered carbon as versatile anodes for sodium-ion batteries. ChemistrySelect 2020;5:1846–57.
[268] Su C, Ru Q, Gao Y, Shi Z, Zheng M, Chen F, et al. Biowaste-sustained $MoSe_2$ composite as an efficient anode for sodium/potassium storage applications. J Alloys Compd 2021;850:156770.
[269] Beda A, Le Meins J-M, Taberna P-L, Simon P, Matei Ghimbeu C. Impact of biomass inorganic impurities on hard carbon properties and performance in Na-ion batteries. Sustainable Materials and Technologies 2020;26:e00227.
[270] Susanti RF, Alvin S, Kim J. Toward high-performance hard carbon as an anode for sodium-ion batteries: demineralization of biomass as a critical step. J Ind Eng Chem 2020;91:317–29.
[271] Dou X, Hasa I, Saurel D, Jauregui M, Buchholz D, Rojo T, et al. Impact of the acid treatment on lignocellulosic biomass hard carbon for sodium-ion battery anodes. ChemSusChem 2018;11:3276–85.
[272] Feng Y, Tao L, He Y, Jin Q, Kuai C, Zheng Y, et al. Chemical-enzymatic fractionation to unlock the potential of biomass-derived carbon materials for sodium ion batteries. J Mater Chem A 2019;7:26954–65.
[273] Hong K, Qie L, Zeng R, Yi Z, Zhang W, Wang D, et al. Biomass derived hard carbon used as a high performance anode material for sodium ion batteries. J Mater Chem A 2014;2:12733–8.
[274] Li C, Li J, Zhang Y, Cui X, Lei H, Li G. Heteroatom-doped hierarchically porous carbons derived from cucumber stem as high-performance anodes for sodium-ion batteries. J Mater Sci 2019;54:5641–57.
[275] Sahu A, Sen S, Mishra SC. Economical way of processing activated carbon from Calotropis gigantea and its suitability for application in Lithium/Sodium ion batteries. Diam Relat Mater 2020;108:107931.
[276] Simões dos Reis G, Mayandi Subramaniyam C, Cárdenas AD, Larsson SH, Thyrel M, Lassi U, et al. Facile synthesis of sustainable activated biochars with different pore structures as efficient additive-carbon-free anodes for lithium-and sodium-ion batteries. ACS Omega 2022;7:42570–81.
[277] Kang B, Chen X, Zeng L, Luo F, Li X, Xu L, et al. In situ fabrication of ultrathin few-layered WSe2 anchored on N, P dual-doped carbon by bioreactor for half/full sodium/potassium-ion batteries with ultralong cycling lifespan. J Colloid Interface Sci 2020;574:217–28.
[278] Wang C, Huang J, Li Q, Cao L, Li J, Kajiyoshi K. Catalyzing carbon surface by Ni to improve initial coulombic efficiency of sodium-ion batteries. J Energy Storage 2020;32:101868.
[279] Xiao N, Zhang X, Liu C, Wang Y, Li H, Qiu J. Coal-based carbon anodes for high-performance potassium-ion batteries. Carbon 2019;147:574–81.
[280] Chen Y, Guo X, Liu A, Zhu H, Ma T. Recent progress in biomass-derived carbon materials used for secondary batteries. Sustain Energy Fuels 2021;5:3017–38.
[281] Zhu Z, Xu Z. The rational design of biomass-derived carbon materials towards next-generation energy storage: a review. Renew Sustain Energy Rev 2020;134:110308.
[282] Kim H, Kim JC, Bianchini M, Seo DH, Rodriguez-Garcia J, Ceder G. Recent progress and perspective in electrode materials for K-ion batteries. Adv Energy Mater 2018;8:1702384.
[283] Zhao J, Zou X, Zhu Y, Xu Y, Wang C. Electrochemical intercalation of potassium into graphite. Adv Funct Mater 2016;26:8103–10.
[284] Li X, Zhou Y, Deng B, Li J, Xiao Z. Research progress of biomass carbon materials as anode materials for potassium-ion batteries. Front Chem 2023;11:1162909.
[285] Reis GSD, Petnikota S, Subramaniyam CM, de Oliveira HP, Larsson S, Thyrel M, et al. Sustainable biomass-derived carbon electrodes for potassium and aluminum batteries: conceptualizing the key parameters for improved performance. Nanomaterials 2023;13:765.
[286] Yuan X, Zhu B, Feng J, Wang C, Cai X, Qin R. Recent advance of biomass-derived carbon as anode for sustainable potassium ion battery. Chem Eng J 2021;405:126897.
[287] Zhang Z, Jia B, Liu L, Zhao Y, Wu H, Qin M, et al. Hollow multihole carbon bowls: a stress–release structure design for high-stability and high-volumetric-capacity potassium-ion batteries. ACS Nano 2019;13:11363–71.
[288] Lu J-F, Li K-C, Lv X-Y, Lei F-H, Mi Y, Wen Y-X. N-doped pinecone-based carbon with a hierarchical porous pie-like structure: a long-cycle-life anode material for potassium-ion batteries. RSC Adv 2022;12:20305–18.
[289] Yang M, Kong Q, Feng W, Yao W, Wang Q. Hierarchical porous nitrogen, oxygen, and phosphorus ternary doped hollow biomass carbon spheres for high-speed and long-life potassium storage. Carbon Energy 2022;4:45–59.
[290] He J, Manthiram A. A review on the status and challenges of electrocatalysts in lithium-sulfur batteries. Energy Storage Mater 2019;20:55–70.
[291] Benítez A, Amaro-Gahete J, Chien Y-C, Caballero Á, Morales J, Brandell D. Recent advances in lithium-sulfur batteries using biomass-derived carbons as sulfur host. Renew Sustain Energy Rev 2022;154:111783.
[292] Tian X, Yan C, Kang J, Yang X, Li Q, Yan J, et al. Working mechanisms and structure engineering of renewable biomass-derived materials for advanced lithium-sulfur batteries: a review. Chemelectrochem 2022;9:e202100995.
[293] Ma C, Zhang M, Ding Y, Xue Y, Wang H, Li P, et al. Green production of biomass-derived carbon materials for high-performance lithium–sulfur batteries. Nanomaterials 2023;13:1768.
[294] Zhang S, Zheng M, Lin Z, Li N, Liu Y, Zhao B, et al. Activated carbon with ultrahigh specific surface area synthesized from natural plant material for lithium–sulfur batteries. J Mater Chem A 2014;2:15889–96.
[295] Chung SH, Manthiram A. Carbonized eggshell membrane as a natural polysulfide reservoir for highly reversible Li-S batteries. Adv Mater 2014;26:1360–5.
[296] Ji X, Lee KT, Nazar LF. A highly ordered nanostructured carbon–sulphur cathode for lithium–sulphur batteries. Nat Mater 2009;8:500–6.
[297] Yang J, Wang G, Teixeira AP, Silva GG, Hansen Z, Jamal MJM, et al. A biomass-based cathode for long-life lithium-sulfur batteries. Electrochem Commun 2022;140:107325.
[298] Zhang M, Lu C, Bi Z, Xu X, Ren X, Li X, et al. Preparation of highly Pyrrolic-nitrogen-doped carbon aerogels for lithium-sulfur batteries. Chemelectrochem 2021;8:895–902.
[299] Xu G, Han J, Ding B, Nie P, Pan J, Dou H, et al. Biomass-derived porous carbon materials with sulfur and nitrogen dual-doping for energy storage. Green Chem 2015;17:1668–74.
[300] Yuan X, Wu L, He X, Zeinu K, Huang L, Zhu X, et al. Separator modified with N, S co-doped mesoporous carbon using egg shell as template for high performance lithium-sulfur batteries. Chem Eng J 2017;320:178–88.
[301] Song Z, Lu X, Hu Q, Ren J, Zhang W, Zheng Q, et al. Synergistic confining polysulfides by rational design a N/P co-doped carbon as sulfur host and functional interlayer for high-performance lithium–sulfur batteries. J Power Sources 2019;421:23–31.
[302] Wang Z, Xu X, Ji S, Liu Z, Zhang D, Shen J, et al. Recent progress of flexible sulfur cathode based on carbon host for lithium-sulfur batteries. J Mater Sci Technol 2020;55:56–72.
[303] Yan S, Wu J, Dai Y, Pan Z, Sheng W, Xu J, et al. Excellent electrochemical application of Ni-based hydroxide/biomass porous carbon/sulfur composite cathode on lithium-sulfur batteries. Colloids Surf A Physicochem Eng Asp 2020;591:124513.
[304] Lei W, Wang X, Zhang Y, Luo Z, Xia P, Zou Y, et al. Facile synthesis of Fe3C nano-particles/porous biochar cathode materials for lithium sulfur battery. J Alloys Compd 2021;853:157024.
[305] Wang X, Zhang Y, Chang Q, Wu Y, Lei W, Zou Y, et al. Porous biochar nanosheets loaded with Fe3C particles accelerate electrochemical reactions and their applications in Li–S batteries. Sustain Energy Fuels 2021;5:4346–54.
[306] Lin Y, He S, Ouyang Z, Li J, Zhao J, Xiao Y, et al. Synergistic engineering of cobalt selenide and biomass-derived S, N, P co-doped hierarchical porous carbon for modulation of stable Li-S batteries. J Mater Sci Technol 2023;134:11–21.
[307] Hartmann P, Bender CL, Vračar M, Dürr AK, Garsuch A, Janek J, et al. A rechargeable room-temperature sodium superoxide (NaO2) battery. Nat Mater 2013;12:228–32.
[308] Wang H-F, Xu Q. Materials design for rechargeable metal-air batteries. Matter 2019;1:565–95.
[309] Shui J, Du F, Xue C, Li Q, Dai L. Vertically aligned N-doped coral-like carbon fiber arrays as efficient air electrodes for high-performance nonaqueous Li–O2 batteries. ACS Nano 2014;8:3015–22.
[310] Wang Y, Hao J, Yu J, Yu H, Wang K, Yang X, et al. Hierarchically porous N-doped carbon derived from biomass as oxygen reduction electrocatalyst for high-performance Al–air battery. J Energy Chem 2020;45:119–25.
[311] Cheng R, Yang J, Jiang M, Dong A, Guo M, Zhang J, et al. Hierarchical porous manganese-and nitrogen-codoped carbon nanosheets derived from surface modified biomass as efficient oxygen reduction catalysts for Al-air batteries. J Electrochem Soc 2020;167:110552.
[312] Zhao C, Liu G, Sun N, Zhang X, Wang G, Zhang Y, et al. Biomass-derived N-doped porous carbon as electrode materials for Zn-air battery powered capacitive deionization. Chem Eng J 2018;334:1270–80.
[313] Kim M-J, Park JE, Kim S, Lim MS, Jin A, Kim O-H, et al. Biomass-derived air cathode materials: pore-controlled S, N-co-doped carbon for fuel cells and metal–air batteries. ACS Catal 2019;9:3389–98.
[314] Liang H, Jia L, Chen F. Three-dimensional self-standing Co@ NC octahedron/biochar cathode for non-aqueous Li-O2 batteries: efficient catalysis for reversible formation and decomposition of LiOH. J Mater Sci 2020;55:7792–804.
[315] Wang Y, Yu B, Liu K, Yang X, Liu M, Chan T-S, et al. Co single-atoms on ultrathin N-doped porous carbon via a biomass complexation strategy for high performance metal–air batteries. J Mater Chem A 2020;8:2131–9.
[316] Zago S, Bartoli M, Muhyuddin M, Vanacore GM, Jagdale P, Tagliaferro A, et al. Engineered biochar derived from pyrolyzed waste tea as a carbon support for Fe-

NC electrocatalysts for the oxygen reduction reaction. Electrochim Acta 2022; 412:140128.
[317] Jing S, Gai Z, Li M, Tang S, Ji S, Liang H, et al. Enhanced electrochemical performance of a Li-O2 battery using Co and N co-doped biochar cathode prepared in molten salt medium. Electrochim Acta 2022;410:140002.
[318] Crabtree G. Perspective: the energy-storage revolution. Nature 2015;526:S92.
[319] Schneider SF, Bauer C, Novák P, Berg EJ. A modeling framework to assess specific energy, costs and environmental impacts of Li-ion and Na-ion batteries. Sustain Energy Fuels 2019;3:3061–70.
[320] Kane S, Storer A, Xu W, Ryan C, Stadie NP. Biochar as a renewable Substitute for carbon black in lithium-ion battery electrodes. ACS Sustainable Chem Eng 2022; 10:12226–33.
[321] Maroušek J, Vochozka M, Plachý J, Žák J. Glory and misery of biochar. Clean Technol Environ Policy 2017;19:311–7.
[322] Montanarella L, Lugato E. The application of biochar in the EU: challenges and opportunities. Agronomy 2013;3:462–73.
[323] Matovic D. Biochar as a viable carbon sequestration option: Global and Canadian perspective. Energy 2011;36:2011–6.
[324] Anand A, Kumar V, Kaushal P. Biochar and its twin benefits: crop residue management and climate change mitigation in India. Renew Sustain Energy Rev 2022;156:111959.
[325] Gwenzi W, Chaukura N, Mukome FN, Machado S, Nyamasoka B. Biochar production and applications in sub-Saharan Africa: opportunities, constraints, risks and uncertainties. J Environ Manag 2015;150:250–61.
[326] Matuštík J, Pohořelý M, Kočí V. Is application of biochar to soil really carbon negative? The effect of methodological decisions in Life Cycle Assessment. Sci Total Environ 2022;807:151058.
[327] Tisserant A, Morales M, Cavalett O, O'Toole A, Weldon S, Rasse DP, et al. Life-cycle assessment to unravel co-benefits and trade-offs of large-scale biochar deployment in Norwegian agriculture. Resour Conserv Recycl 2022;179:106030.
[328] Puettmann M, Sahoo K, Wilson K, Oneil E. Life cycle assessment of biochar produced from forest residues using portable systems. J Clean Prod 2020;250: 119564.
[329] Bergman R, Sahoo K, Englund K, Mousavi-Avval SH. Lifecycle assessment and techno-economic analysis of biochar pellet production from forest residues and field application. Energies 2022;15:1559.